

AD _____

Grant Number DAMD17-96-1-6093

TITLE: An Overcomplete Enhancement of Digital Mammograms

PRINCIPAL INVESTIGATOR: Fred Taylor, Ph.D.
Iztok Koren, Ph.D.

CONTRACTING ORGANIZATION: University of Florida
Gainesville, Florida 32611

REPORT DATE: August 1999

TYPE OF REPORT: Final

PREPARED FOR: U.S. Army Medical Research and Materiel Command
Fort Detrick, Maryland 21702-5012

DISTRIBUTION STATEMENT: Approved for public release;
distribution unlimited

The views, opinions and/or findings contained in this report are those of the author(s) and should not be construed as an official Department of the Army position, policy or decision unless so designated by other documentation.

DTIC QUALITY INSPECTED 4

20010122 102

REPORT DOCUMENTATION PAGE

Form Approved

OMB No. 0704-0188

Public reporting burden for this collection of information is estimated to average 1 hour per response, including the time for reviewing instructions, searching existing data sources, gathering and maintaining the data needed, and completing and reviewing the collection of information. Send comments regarding this burden estimate or any other aspect of this collection of information, including suggestions for reducing this burden, to Washington Headquarters Services, Directorate for Information Operations and Reports, 1215 Jefferson Davis Highway, Suite 1204, Arlington, VA 22202-4302, and to the Office of Management and Budget, Paperwork Reduction Project (0704-0188), Washington, DC 20503.

1. AGENCY USE ONLY (Leave blank)		2. REPORT DATE August 1999	3. REPORT TYPE AND DATES COVERED Final (1 Aug 96 - 31 Jul 99)	
4. TITLE AND SUBTITLE An Overcomplete Enhancement of Digital Mammograms			5. FUNDING NUMBERS DAMD17-96-1-6093	
6. AUTHOR(S) Fred Taylor, Ph.D. Iztok Koren, Ph.D.				
7. PERFORMING ORGANIZATION NAME(S) AND ADDRESS(ES) University of Florida Gainesville, FL 32611			8. PERFORMING ORGANIZATION REPORT NUMBER	
9. SPONSORING/MONITORING AGENCY NAME(S) AND ADDRESS(ES) U.S. Army Medical Research and Materiel Command Fort Detrick, Frederick, Maryland 21702-5012			10. SPONSORING/MONITORING AGENCY REPORT NUMBER	
11. SUPPLEMENTARY NOTES				
12a. DISTRIBUTION / AVAILABILITY STATEMENT Approved for public release; distribution unlimited			12b. DISTRIBUTION CODE	
13. ABSTRACT (Maximum 200) <p>This report deals with a technique for contrast enhancement of mammographic images by means of image fusion. We constructed a multiscale directional derivative based redundant wavelet representation to serve as a framework for image enhancement without introducing artifacts that could distort the appearance of mammographic features. After the wavelet decomposition is carried out, the transform coefficients are separately processed for enhancement of microcalcifications, circumscribed masses, and stellate lesions, and then fused for reconstruction of an image with improved visibility of mammographic abnormalities. Since the processing for enhancement of selected features and fusion of the resultant images are accomplished within a single wavelet transform framework, the method is computationally efficient and flexible enough for incorporation of different enhancement algorithms and their independent optimization.</p> <p>In order to evaluate the performance of the developed technique, we used quantitative criteria for comparison with histogram equalization and unsharp masking. Our method outperformed the two enhancement approaches during tests on simulated phantoms embedded in noise and on mammographic feature phantoms blended into mammograms. In addition, no spurious artifacts were observed as a result of our redundant wavelet transform based contrast enhancement scheme.</p>				
14. SUBJECT TERMS Breast Cancer			15. NUMBER OF PAGES 62	
			16. PRICE CODE	
17. SECURITY CLASSIFICATION OF REPORT Unclassified	18. SECURITY CLASSIFICATION OF THIS PAGE Unclassified	19. SECURITY CLASSIFICATION OF ABSTRACT Unclassified	20. LIMITATION OF ABSTRACT Unlimited	

FOREWORD

Opinions, interpretations, conclusions and recommendations are those of the author and are not necessarily endorsed by the U.S. Army.

____ Where copyrighted material is quoted, permission has been obtained to use such material.

____ Where material from documents designated for limited distribution is quoted, permission has been obtained to use the material.

✓ Citations of commercial organizations and trade names in this report do not constitute an official Department of Army endorsement or approval of the products or services of these organizations.

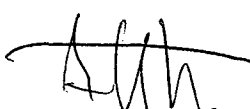
N/A In conducting research using animals, the investigator(s) adhered to the "Guide for the Care and Use of Laboratory Animals," prepared by the Committee on Care and use of Laboratory Animals of the Institute of Laboratory Resources, national Research Council (NIH Publication No. 86-23, Revised 1985).

N/A For the protection of human subjects, the investigator(s) adhered to policies of applicable Federal Law 45 CFR 46.

N/A In conducting research utilizing recombinant DNA technology, the investigator(s) adhered to current guidelines promulgated by the National Institutes of Health.

N/A In the conduct of research utilizing recombinant DNA, the investigator(s) adhered to the NIH Guidelines for Research Involving Recombinant DNA Molecules.

N/A In the conduct of research involving hazardous organisms, the investigator(s) adhered to the CDC-NIH Guide for Biosafety in Microbiological and Biomedical Laboratories.


PI - Signature

01/31/2000
Date

Table of Contents

1	Introduction	7
1.1	Overview of Contents	7
1.2	Notation	8
2	Body	10
2.1	Wavelet Transform	10
2.1.1	Shortcomings of Traditional Methods of Wavelet Analysis	10
2.1.2	Multiscale Spline Derivatives	13
2.1.3	Filter Implementations	19
2.2	Image Fusion	25
2.2.1	Comparison of Transforms	25
2.2.2	Fusion of Enhanced Features	33
2.3	Evaluation	40
2.3.1	Image Phantoms	42
2.3.2	Phantoms Blended Into Mammograms	45
3	Key Research Accomplishments	54
4	Reportable Outcomes	55
5	Conclusions	56
	References	58
	List of Personnel	62

List of Tables

1	Transfer functions of direct B-spline filters for orders from 0 to 9.	17
2	Impulse responses $g^1(n)$ and $g^2(n)$	18
3	Impulse responses $h(n)$, $k^1(n)$, $k^2(n)$, and $t(n)$ for $p=0$	18
4	Impulse responses $h(n)$, $k^1(n)$, $k^2(n)$, and $t(n)$ for $p=1$	18
5	Impulse responses $h(n)$, $k^1(n)$, $k^2(n)$, and $t(n)$ for $p=2$	18
6	Performance of fusion algorithms based on four different transforms.	29
7	Quantitative assessment of contrast enhancement of image phantoms.	44
8	Quantitative assessment of contrast enhancement of mass phantoms.	52
9	Quantitative assessment of contrast enhancement of micros phantoms.	52
10	Quantitative assessment of contrast enhancement of spiculate lesion phantoms.	53

List of Figures

1	Discrete wavelet transform of two signals translated to each other.	12
2	Discrete wavelet transform and "algorithm à trous."	13
3	Filter bank implementation of multiscale spline derivatives.	17
4	Spline derivatives in the x -axis direction.	19
5	Phantom used for comparisons of different transforms for image fusion. . . .	28
6	Image fusion of phantoms shifted by one sample.	30
7	Image fusion of phantoms shifted by five samples.	31
8	Blurred mammograms for evaluation of fusion algorithms.	32
9	Zooming in on the region of interest in the fused images.	34
10	Overview of the algorithm.	35
11	Enhancement function.	38
12	Local enhancement of a circumscribed mass.	39
13	Local enhancement of a stellate lesion.	41
14	Image phantom used for comparison of contrast enhancement methods. . . .	43
15	Contrast enhancement of a moderately noisy image phantom.	46
16	Contrast enhancement of a low contrast, noisy image phantom.	47
17	Mathematical phantoms that were blended into mammographic images. . . .	48
18	Contrast enhancement of a mass resembling phantom.	49
19	Contrast enhancement of a microcalcifications resembling phantom.	50
20	Contrast enhancement of a microcalcifications resembling phantom.	51

1 Introduction

Breast cancer is the most frequently diagnosed malignancy among women in the United States. In 1999, the American Cancer Society estimated that 175,000 women would be newly diagnosed with breast cancer and that 43,300 would die from the disease [1]. Breast cancer accounts for 29% of all cancers detected and 16% of all cancer deaths, and ranks as the second leading cause of death from cancer among women in the United States [1]. Five year survival rates are generally very high (93%) for breast cancer staged as being localized, falling to 72% for regional disease and only 18% for distant disease [2]. The early detection of breast cancer is clearly a key ingredient of any strategy designed to reduce breast cancer mortality.

The goal of this project was to develop computerized tools that will refine the perception of mammographic features (including lesions, masses and calcifications). Our research efforts were geared towards improving the local mammographic viewing environment by selectively processing mammograms for presence of different features, and towards providing a better global mammographic viewing environment by fusing together locally processed sections of images. By improving the visualization of breast pathology, the chances of early detection of breast cancers can be increased (quality improved) while less time to evaluate mammograms for most patients required (costs lowered).

We were investigating a methodology for accomplishing mammographic feature analysis through multiscale representations. In this report, we present a scheme for local enhancement and fusion of clinically significant features. We devised a wavelet transform that is flexible enough for incorporation of a variety of enhancement methods and used the derived wavelet framework for enhancement of microcalcifications, circumscribed masses, and stellate lesions.

In the following sections, we briefly overview the contents of the report, list publications, and explain notation that we use.

1.1 Overview of Contents

Wavelet transform forms the framework of our contrast enhancement technique, and Section 2.1 is dedicated to it. First, Section 2.1.1 motivates the use of redundant representations instead of orthogonal and biorthogonal wavelet transforms. The transform itself is then described in Section 2.1.2, while Section 2.1.3 deals with fast transform implementations issues.

Mammographic image enhancement methods are typically aimed at either improvement of the overall visibility of features or enhancement of a specific sign of malignancy. Section 2.2

presents a synthesis of the two paradigms by means of image fusion. In Section 2.2.1, the suitability of steerable dyadic wavelet transform for image fusion was compared to two transforms popular in fusion applications, the gradient pyramid and orthogonal/biorthogonal wavelet transform, by means of both subjective and objective criteria. Section 2.2.2 next reports on local enhancement strategies targeting microcalcifications, circumscribed masses, and stellate lesions.

Evaluation of our method is presented in Section 2.3. The method was compared to histogram equalization and unsharp masking on image phantoms in Section 2.3.1 and on phantoms blended into mammograms in Section 2.3.2. The comparisons were performed using objective measures, but behavior of the three techniques was assessed from the perceptual point of view as well.

1.2 Notation

We use symbols \mathbf{N} , \mathbf{Z} , and \mathbf{R} for the sets of naturals, integers, and reals, respectively. $L^2(\mathbf{R})$ and $L^2(\mathbf{R}^2)$ denote the Hilbert spaces of measurable, square-integrable functions $f(x)$ and $f(x, y)$, respectively.

The inner product of two functions $f(x) \in L^2(\mathbf{R})$ and $g(x) \in L^2(\mathbf{R})$ is given by

$$\langle f(x), g(x) \rangle = \int_{-\infty}^{\infty} f(x) g(x) dx.$$

The norm of a function $f(x) \in L^2(\mathbf{R})$ is defined as

$$\|f\| = \sqrt{\int_{-\infty}^{\infty} |f(x)|^2 dx}.$$

The convolution of functions $f(x) \in L^2(\mathbf{R})$ and $g(x) \in L^2(\mathbf{R})$ is computed as

$$f * g(x) = \int_{-\infty}^{\infty} f(t) g(x - t) dt,$$

and the convolution of two functions $f(x, y) \in L^2(\mathbf{R}^2)$ and $g(x, y) \in L^2(\mathbf{R}^2)$ equals

$$f * g(x, y) = \int_{-\infty}^{\infty} \int_{-\infty}^{\infty} f(t_x, t_y) g(x - t_x, y - t_y) dt_x dt_y.$$

The Fourier transform of a function $f(x) \in L^2(\mathbf{R})$ is defined as

$$\hat{f}(\omega) = \int_{-\infty}^{\infty} f(x) e^{-j\omega x} dx,$$

and the Fourier transform of a function $f(x, y) \in L^2(\mathbf{R}^2)$ is equal to

$$\hat{f}(\omega_x, \omega_y) = \int_{-\infty}^{\infty} \int_{-\infty}^{\infty} f(x, y) e^{-j(\omega_x x + \omega_y y)} dx dy.$$

$l^2(\mathbf{Z})$ and $l^2(\mathbf{Z}^2)$ stand for the spaces of square-summable discrete signals $f(n)$ and $f(n_x, n_y)$, respectively.

The z -transform of a discrete signal $f(n) \in l^2(\mathbf{Z})$ is defined as

$$F(z) = \sum_{n=-\infty}^{\infty} f(n)z^{-n}.$$

The convolution of discrete signals $f(n) \in l^2(\mathbf{Z})$ and $g(n) \in l^2(\mathbf{Z})$ is equal to

$$f * g(n) = \sum_{m=-\infty}^{\infty} f(m)g(n-m),$$

and the convolution of discrete signals $f(n_x, n_y) \in l^2(\mathbf{Z}^2)$ and $g(n_x, n_y) \in l^2(\mathbf{Z}^2)$ is given by

$$f * g(n_x, n_y) = \sum_{m_x=-\infty}^{\infty} \sum_{m_y=-\infty}^{\infty} f(m_x, m_y)g(n_x - m_x, n_y - m_y).$$

The Fourier transform of a discrete signal $f(n) \in l^2(\mathbf{Z})$ is equal to the z -transform evaluated on the unit circle

$$F(\omega) = \sum_{n=-\infty}^{\infty} f(n)e^{-j\omega n},$$

and the Fourier transform of a discrete signal $f(n_x, n_y) \in l^2(\mathbf{Z}^2)$ is defined as

$$F(\omega_x, \omega_y) = \sum_{n_x=-\infty}^{\infty} \sum_{n_y=-\infty}^{\infty} f(n_x, n_y) e^{-j(\omega_x n_x + \omega_y n_y)}.$$

For later use, we define the following functions:

1. the unit impulse function

$$\delta_u(x) := \begin{cases} 1 & \text{for } x = 0 \\ 0 & \text{otherwise,} \end{cases}$$

2. the unit step function

$$u(x) := \begin{cases} 1 & \text{for } x \geq 0 \\ 0 & \text{for } x < 0, \end{cases}$$

3. the rectangular function

$$\text{rect}(x) := \begin{cases} 1 & \text{for } |x| \leq \frac{1}{2} \\ 0 & \text{for } |x| > \frac{1}{2}, \end{cases}$$

4. the sinc function

$$\text{sinc}(x) := \frac{\sin(\pi x)}{\pi x}, \quad \text{and}$$

5. the unit impulse sequence

$$\delta(n) := \begin{cases} 1 & \text{for } n = 0 \\ 0 & \text{otherwise,} \end{cases}$$

where $x \in \mathbf{R}$ and $n \in \mathbf{Z}$.

2 Body

2.1 Wavelet Transform

Wavelet transform provides the framework for both our enhancement and fusion algorithms, and it is, therefore, important that it does not introduce artifacts, enables directional multiscale analysis, and can be implemented efficiently. In Section 2.1.1, we mention problems that stem from the lack of translation and rotation invariance of orthogonal and biorthogonal wavelet transforms. Next, in Section 2.1.2, we describe approximations of steerable wavelets and employ the multiscale spline derivatives with both first and second derivative wavelet decomposition. Our annual reports contain details on higher order transform derivation and implementation with reconstruction (*i.e.*, inverse transform) being quite cumbersome. Here presented transform allows for both directional and isotropic processing of mammograms while being shift-invariant and aliasing-free. Efficient implementation of the transform is highly desirable, and Section 2.1.3 presents a filter bank with filter implementations taking advantage of symmetry and antisymmetry for faster processing.

2.1.1 Shortcomings of Traditional Methods of Wavelet Analysis

Analyzing images across multiple scales and resolution has become a powerful tool for solving compelling problems in computational vision, image processing, and pattern recognition. Wavelet theory encompasses multiscale and multiresolution representations, such as subband filtering [3], image pyramids [4], and scale space filtering [5], into a unified mathematical framework. In the area of image processing, there remain few research areas to which wavelet analysis has not been applied. For example, problems in image compression, denoising, restoration, enhancement, registration, fusion, segmentation, and analysis, have all been approached with distinct kinds of wavelet processing.

Though ubiquitous, wavelet analysis is not without problems of its own. Lack of translation invariance, one of the major problems of the wavelet transform [6], is in multiple dimensions accompanied with lack of rotation invariance.

Wavelet transform in its most commonly used orthogonal or biorthogonal forms is not translation and rotation-invariant. By translation-invariant transform, we mean a transform that commutes with a translation operator. Since we will deal primarily with discrete transforms in this work, we constrain the translation parameter to integer multiples of a sampling period.

Lack of translation invariance of the discrete wavelet transform is illustrated in Figure 1. Here, we can clearly see how a translation of the input signal by one sample results in a

completely different set of transform coefficients (orthogonal wavelet DAUB4¹ [6] was used in this experiment).

Noninvariance under translations of an orthogonal and biorthogonal wavelet transform is due to lower sampling density at coarser scales.² A straightforward way of dealing with this problem is to construct a redundant transform by using the same sampling frequency for the input signal and all scales of the transform. A filter bank implementation of such a transform, called “*algorithme à trous*” [7], is based upon the fact that downsampling followed by filtering is equivalent to filtering with the upsampled filter before the downsampling, as shown in Figure 2.

Lack of rotation invariance is another shortcoming of traditional (i.e., orthogonal and biorthogonal) wavelet techniques. In defining rotation invariance, we are a bit less strict than with translation invariance. We do not require that the transform commutes with a rotation operator here. Even in the case of a simple filtering, this would limit us to circularly symmetric filters only. Our requirement for analysis is a transform that enables rotation-invariant processing. As an example of such a transform, let us consider filtering with the first derivative of a two-dimensional Gaussian probability density function in two directions, specifically, along x and along y -axis. By linearly combining the results of filtering in these two directions, filtering with the first derivative of a Gaussian in any direction can be computed. This fact was used by Canny [8] for edge detection. A determined edge direction rotates as an input image is rotated.

After choosing the fundamental properties of the transform, one must decide upon the basis functions to be applied. For our studies, we selected basis functions that well approximated derivatives of a Gaussian, because (1) the Gaussian probability density function is optimally concentrated in both time and frequency domain, and thus suitable for time-frequency analysis, (2) higher order derivatives of a Gaussian can be, similar to the first derivative, used for rotation-invariant processing [9], and (3) the Gaussian function generates a causal (in a sense that a coarse scale depends exclusively on the previous finer scale) scale space [10]. The last property makes possible scale-space “tracking” of emergent features.

¹The number in DAUB4 refers to twice the order of the wavelet (i.e., two in this case).

²In practice, since analysis is performed over a finite range of scales, a discrete wavelet transform is translation-invariant by translations determined by the coarsest scale (e.g., sixteen samples for the analysis from Figure 1) [6].

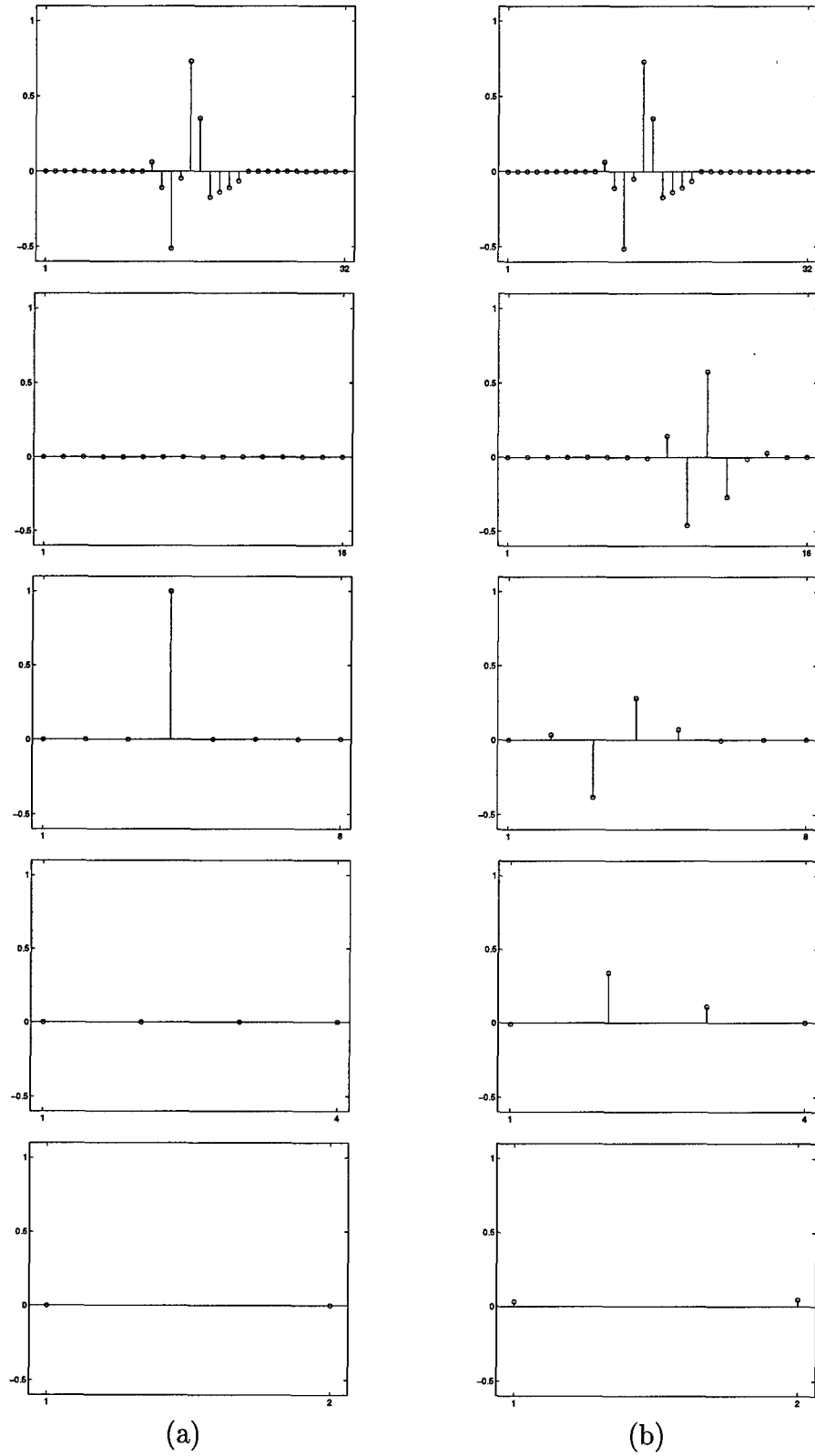


Figure 1: (a) Original signal and (b) signal translated one sample to the left with its discrete wavelet transform coefficients shown across dyadic scales 2^m , $m \in \{1, 2, 3, 4\}$.

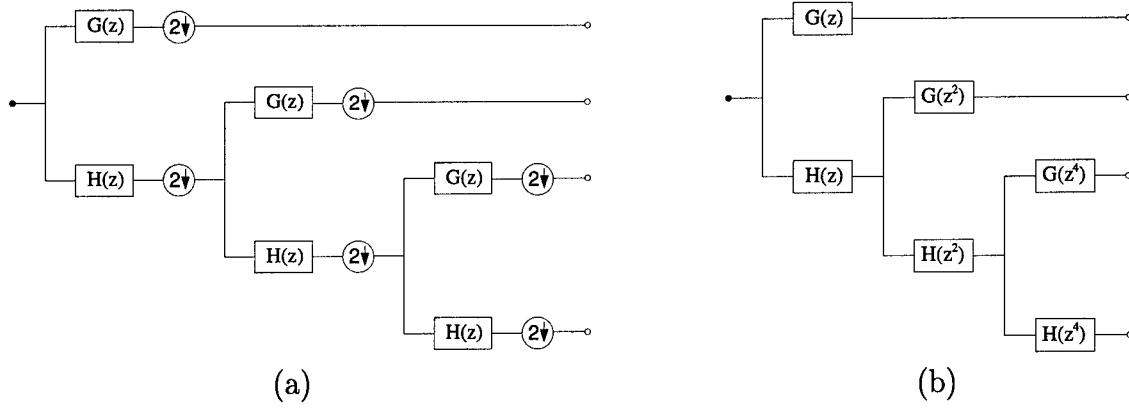


Figure 2: Filter bank implementation for (a) a discrete wavelet transform and (b) “algorithm à trous” decompositions for three levels of analysis.

2.1.2 Multiscale Spline Derivatives

We define a steerable dyadic wavelet transform of a function $s(x, y) \in L^2(\mathbf{R}^2)$ at a scale 2^m , $m \in \mathbf{Z}$, as [11]

$$W_{2^m}^i s(x, y) = s * \psi_{2^m}^i(x, y), \quad (1)$$

where $\psi_{2^m}^i(x, y)$ denotes $\psi_{2^m}(x, y)$ rotated by θ_i , $\psi_{2^m}(x, y) = 2^{-2m}\psi(2^{-m}x, 2^{-m}y)$, $\psi(x, y)$ is a steerable wavelet that can be steered with I basis functions, and $\theta_i = \frac{i-1}{I}\pi$ with $i \in \{1, 2, \dots, I\}$. (For introduction to steerability, please refer to our first annual report.)

Analogous to the one-dimensional case, we require the two-dimensional Fourier plane to be covered by the dyadic dilations of $\hat{\psi}^i(2^m\omega_x, 2^m\omega_y)$: there must exist $A_3 > 0$ and $B_3 < \infty$ such that

$$A_3 \leq \sum_{m=-\infty}^{\infty} \sum_{i=1}^I |\hat{\psi}^i(2^m\omega_x, 2^m\omega_y)|^2 \leq B_3 \quad (2)$$

is satisfied almost everywhere.

If (nonunique) reconstructing functions $\chi_{2^m}^i(x, y)$ are chosen such that their Fourier transforms satisfy

$$\sum_{m=-\infty}^{\infty} \sum_{i=1}^I \hat{\psi}^i(2^m\omega_x, 2^m\omega_y) \hat{\chi}^i(2^m\omega_x, 2^m\omega_y) = 1, \quad (3)$$

the function $s(x, y)$ may be reconstructed from its steerable dyadic wavelet transform by

$$s(x, y) = \sum_{m=-\infty}^{\infty} \sum_{i=1}^I W_{2^m}^i s * \chi_{2^m}^i(x, y), \quad (4)$$

where $\chi_{2^m}^i(x, y)$ denotes $\chi_{2^m}(x, y)$ rotated by θ_i and $\chi_{2^m}(x, y) = 2^{-2m}\chi(2^{-m}x, 2^{-m}y)$.

We choose wavelets that are steerable analogs to the one-dimensional derivatives of central B-spline wavelets [12]:

$$\hat{\psi}(\omega_r, \omega_\theta) = (j\omega_r \cos(\omega_\theta))^d \left(\frac{\sin(\frac{\omega_r}{2})}{\frac{\omega_r}{2}} \right)^{p+d+1}, \quad (5)$$

where $\omega_r = \sqrt{\omega_x^2 + \omega_y^2}$, $\omega_\theta = \arg(\omega_x, \omega_y)$, and $d \in \{1, 2\}$. These wavelets can be steered with $d+1$ basis functions.

Wavelets (5) are equal to d -th order derivatives of circularly symmetric spline functions in the direction of x -axis (note that knots for these splines are circles). To implement the transform efficiently, we approximate the wavelets with x - y separable wavelets

$$\psi(x, y) = \frac{d^d \beta_{p+d}(x)}{dx^d} \beta_{p+d}(y), \quad (6)$$

where $\beta_p(x)$ denotes the central B-spline of order p .

Based on the fact that B-splines tend to a Gaussian probability density function as their order increases, it is easy to see that both wavelets (5) and (6) converge to the same functions (i.e., d -th order derivatives of the normalized Gaussian in the direction of x -axis) as $p \rightarrow \infty$. In order to steer wavelets $\psi(x, y)$ given by (6) (note that steering will be only approximate, since these wavelets are not steerable), we need to find basis functions that will approximately steer $\psi(x, y)$. To accomplish this, we take advantage of the property of circularly symmetric functions that rotations of their directional derivatives are equal to directional derivatives in rotated directions:

$$\mathcal{R}_{\theta_0} \left\{ \frac{\partial^d \varrho_c(x, y)}{\partial \vec{n}^d} \right\} = \frac{\partial^d \varrho_c(x, y)}{\partial \vec{n}_{\theta_0}^d},$$

where \mathcal{R}_{θ_0} stands for rotation by θ_0 , $\frac{\partial \varrho_c(x, y)}{\partial \vec{n}} = \vec{n} \cdot \vec{\nabla} \varrho_c(x, y)$, $\varrho_c(x, y)$ is a circularly symmetric function, and \vec{n}_{θ_0} denotes vector $\vec{n} = (\cos \theta, \sin \theta)$ rotated by θ_0 .

Let us choose

$$\varrho(x, y) = \beta_{p+d}(x) \beta_{p+d}(y),$$

which is approximately circularly symmetric function for higher order splines. A rotation of $\psi(x, y) = \frac{\partial^d \varrho(x, y)}{\partial x^d}$ from Equation (6) by θ_0 can therefore be approximated by

$$\psi^{\theta_0}(x, y) \simeq \frac{\partial^d \varrho(x, y)}{\partial \vec{n}^d} = \sum_{i=0}^d \binom{d}{i} n_x^{d-i} n_y^i \frac{d^{d-i} \beta_{p+d}(x)}{dx^{d-i}} \frac{d^i \beta_{p+d}(y)}{dy^i}, \quad (7)$$

where $\vec{n} = (\cos \theta_0, \sin \theta_0) = (n_x, n_y)$. (Note that in case of Gaussian, which is both x - y separable and circularly symmetric, Equation (7) becomes exact.)

To derive an algorithm for the fast computation of the transform, we introduce two smoothing functions such that

$$\hat{\phi}(\omega_x, \omega_y) \hat{\varphi}(\omega_x, \omega_y) = \sum_{m=0}^{\infty} \sum_{i=1}^I \hat{\psi}^i(2^m \omega_x, 2^m \omega_y) \hat{\chi}^i(2^m \omega_x, 2^m \omega_y). \quad (8)$$

Using a set of basis functions (7) that approximately steer wavelets (6), we want to construct a transform such that Equations (1) through (4) and (8) will be valid (superscript i must be viewed now as an index, rather than rotation by θ_i).

Let $F(\omega)$ be a digital filter frequency response and let us denote

$$F_s(\omega) = e^{j\omega s} F(\omega)$$

with s being a filter dependent sampling shift needed to obtain finite impulse response (FIR) filters.

In frequency domain, we can express basis functions from (7) as

$$\hat{\psi}^{i+1}(\omega_x, \omega_y) = G_{-s}^{d-i}(\omega_x) G_{-s}^i(\omega_y) \hat{\beta}_{p+i}(\omega_x) \hat{\beta}_{p+d-i}(\omega_y), \quad i \in \{0, 1, 2\}, \quad (9)$$

where $G^d(\omega)$ is given by

$$G^d(\omega) = e^{j\omega s} \left(2j \sin \left(\frac{\omega}{2} \right) \right)^d, \quad (10)$$

where d is the order of the derivative, $d \in \{1, 2\}$, the sampling shift for filter (10) is $s = \frac{d \bmod 2}{2}$, and $G^0(\omega) = 1$.

Since we are interested in the first and second derivative wavelets, we impose

$$\hat{\varphi}(\omega_x, \omega_y) = \hat{\phi}(\omega_x, \omega_y) = \hat{\beta}_p(\omega_x) \hat{\beta}_p(\omega_y)$$

and choose

$$\hat{\chi}^1(\omega_x, \omega_y) = K_s^2(\omega_x) T(\omega_y) \hat{\beta}_p(\omega_x) \hat{\beta}_{p-2}(\omega_y), \quad (11)$$

$$\hat{\chi}^2(\omega_x, \omega_y) = K_s^1(\omega_x) K_s^1(\omega_y) \hat{\beta}_{p-1}(\omega_x) \hat{\beta}_{p-1}(\omega_y), \quad (12)$$

$$\hat{\chi}^3(\omega_x, \omega_y) = T(\omega_x) K_s^2(\omega_y) \hat{\beta}_{p-2}(\omega_x) \hat{\beta}_p(\omega_y), \quad (13)$$

where

$$K^d(\omega) = \frac{1}{(2j)^d} \left(e^{-j\omega s} \sin \left(\frac{\omega}{2} \right) \right)^{d \bmod 2} \left(\sum_{m=0}^p \left(\cos \left(\frac{\omega}{2} \right) \right)^{2m} \right)^{\lfloor \frac{d+1}{2} \rfloor}, \quad (14)$$

with the sampling shift for $K^d(\omega)$ being the same as the one for $G^d(\omega)$, and

$$T(\omega) = |H(\omega)|^2 \quad (15)$$

with

$$H(\omega) = e^{j\omega s} \left(\cos \left(\frac{\omega}{2} \right) \right)^{p+1}, \quad (16)$$

the sampling shift for $H(\omega)$ being $s = \frac{(p+1) \bmod 2}{2}$.

Using the relation derived in the previous report

$$\hat{\beta}_p(2\omega) = H_{-s}(\omega) \hat{\beta}_p(\omega) \quad (17)$$

together with Equations (9) and (11) through (13) with Equation (8) results in

$$G^2(\omega_x) K^2(\omega_x) T(\omega_y) + G^1(\omega_x) K^1(\omega_x) G^1(\omega_y) K^1(\omega_y) + T(\omega_x) G^2(\omega_y) K^2(\omega_y) + |H(\omega_x) H(\omega_y)|^2 = 1.$$

Next, we derive a filter bank implementation of the transform. Assuming a bandlimited input signal $\hat{s}(\omega_x, \omega_y) = 0$ for $|\omega_x| > \pi$ or $|\omega_y| > \pi$ and using Shannon's sampling theorem in two dimensions [13] with Equation (1) and basis functions from Equation (9), we can write

$$W_1^i s(x, y) = \int_{-\infty}^{\infty} \int_{-\infty}^{\infty} \sum_{i_x=-\infty}^{\infty} \sum_{i_y=-\infty}^{\infty} s(i_x, i_y) \text{sinc}(t_x - i_x) \text{sinc}(t_y - i_y) \cdot \sum_{m_x=-\infty}^{\infty} g_{-s}^{d-i}(m_x) \beta_{p+i}(x - t_x - m_x) \sum_{m_y=-\infty}^{\infty} g_{-s}^i(m_y) \beta_{p+d-i}(y - t_y - m_y) dt_x dt_y,$$

where $i \in \{0, 1, 2\}$ as in Equation (9).

We approximate sinc functions with r -order cardinal splines, then use the relation between cardinal and B-splines

$$\eta_r(x) = \sum_{i=-\infty}^{\infty} b_r^{-1}(i) \beta_r(x - i)$$

and get

$$\mathcal{F}\{W_{2^m}^i s(x, y) \big|_{x=n_x, y=n_y}\} \simeq S(\omega_x, \omega_y) B_r^{-1}(\omega_x) B_r^{-1}(\omega_y) B_{p+r+i+1}(\omega_x) \cdot B_{p+r+d-i+1}(\omega_y) G_{-s}^{d-i}(2^m \omega_x) G_{-s}^i(2^m \omega_y) \prod_{n=0}^{m-1} H_{-s}^{p+i}(2^n \omega_x) H_{-s}^{p+d-i}(2^n \omega_y), \quad (18)$$

where $B_p^{-1}(\omega)$ denotes the Fourier transform of the direct B-spline filter of order p . Table 1 shows the z -transforms of direct B-spline filters for the first ten orders.

Using Equation (18) with an approximation $B_{p+r+i+1}(\omega) \simeq B_{p+r}(\omega) B_i(\omega)$, we can obtain a filter bank implementation of the transform decomposition. The reconstruction part follows from Equations (8), (9), and (11) through (13). Figure 3 shows a filter bank implementation of the transform. Noninteger shifts at scale 1 are rounded to the nearest integer. Tables 2 through 5 list impulse responses of the filters used in the filter bank for $p \in \{0, 1, 2\}$.

Table 1: Transfer functions of direct B-spline filters for orders from 0 to 9.

p	$B_p^{-1}(z)$
0	1
1	1
2	$\frac{8}{z+6+z^{-1}}$
3	$\frac{6}{z+4+z^{-1}}$
4	$\frac{384}{z^2+76z+230+76z^{-1}+z^{-2}}$
5	$\frac{120}{z^2+26z+66+26z^{-1}+z^{-2}}$
6	$\frac{46080}{z^3+722z^2+10543z+23548+10543z^{-1}+722z^{-2}+z^{-3}}$
7	$\frac{5040}{z^3+120z^2+1191z+2416+1191z^{-1}+120z^{-2}+z^{-3}}$
8	$\frac{10321920}{z^4+6552z^3+331612z^2+2485288z+4675014+2485288z^{-1}+331612z^{-2}+6552z^{-3}+z^{-4}}$
9	$\frac{362880}{z^4+502z^3+14608z^2+88234z+156190+88234z^{-1}+14608z^{-2}+502z^{-3}+z^{-4}}$

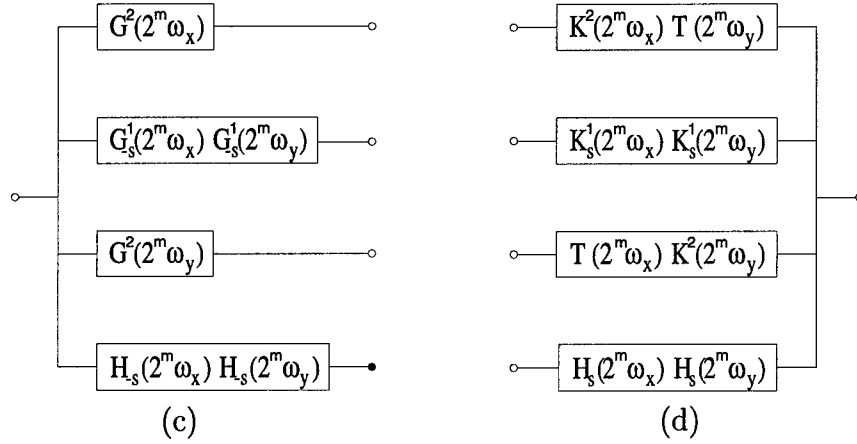
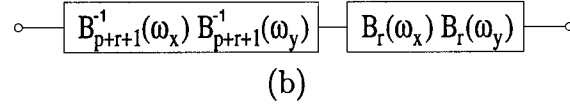
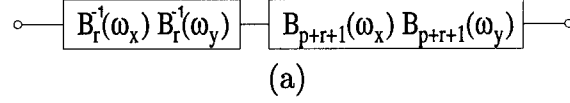


Figure 3: Filter bank implementation of multiscale spline derivatives for $m \in [0, M-1]$: (a) Prefiltering, (b) postfiltering, (c) decomposition module, and (d) reconstruction module.

Table 2: Impulse responses $g^1(n)$ and $g^2(n)$.

n	$g^1(n)$	$g^2(n)$
-1	1	1
0	-1	-2
1		1

Table 3: Impulse responses $h(n)$, $k^1(n)$, $k^2(n)$, and $t(n)$ for $p=0$.

n	$h(n)$	$k^1(n)$	$k^2(n)$	$t(n)$
-1	0.5			0.25
0	0.5	-0.25	-0.25	0.5
1		0.25		0.25

Table 4: Impulse responses $h(n)$, $k^1(n)$, $k^2(n)$, and $t(n)$ for $p=1$.

n	$h(n)$	$k^1(n)$	$k^2(n)$	$t(n)$
-2				0.0625
-1	0.25	-0.0625	-0.0625	0.25
0	0.5	-0.3125	-0.375	0.375
1	0.25	0.3125	-0.0625	0.25
2		0.0625		0.0625

Table 5: Impulse responses $h(n)$, $k^1(n)$, $k^2(n)$, and $t(n)$ for $p=2$.

n	$h(n)$	$k^1(n)$	$k^2(n)$	$t(n)$
-3				0.015625
-2	0.125	-0.015625	-0.015625	0.09375
-1	0.375	-0.109375	-0.125	0.234375
0	0.375	-0.34375	-0.46875	0.3125
1	0.125	0.34375	-0.125	0.234375
2		0.109375	-0.015625	0.09375
3		0.015625		0.015625

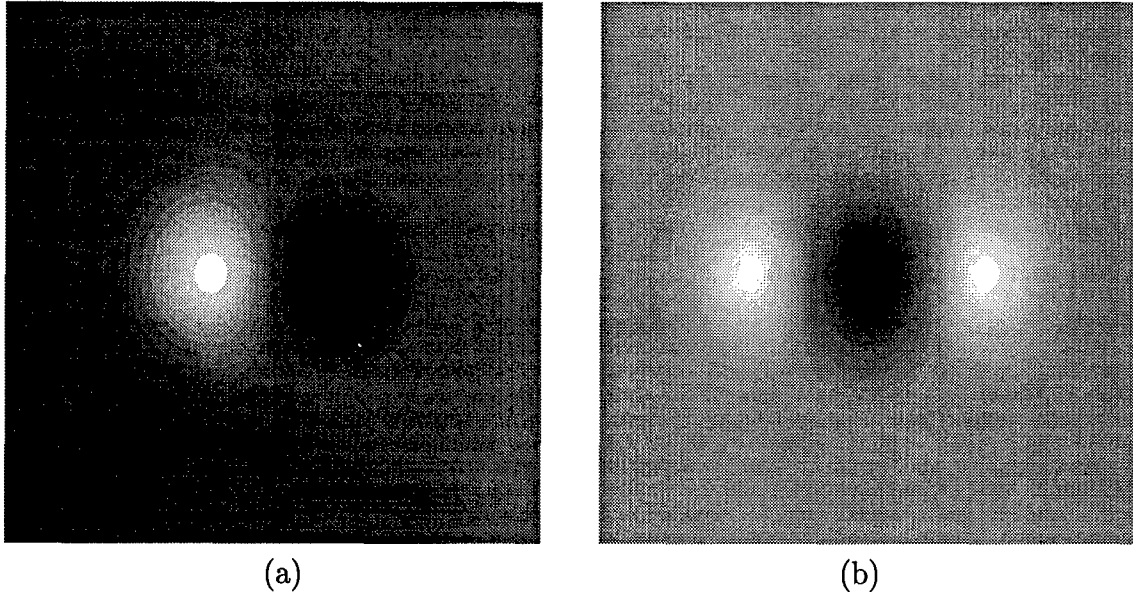


Figure 4: Spline derivatives in the x -axis direction. (a) Wavelet equal to the first derivative of a quartic spline. (b) Wavelet equal to the second derivative of a quintic spline.

The derived transform enables both second derivative directional analysis and Laplacian of Gaussian approximations across dyadic scales (the latter can be obtained through summation of the outputs from blocks $G^2(2^m\omega)$ applied along x and y axis). Furthermore, addition of a block $G_{-s}^1(2^m\omega)$ at each level of decomposition allows first derivative directional analysis as well. Figure 4 shows first and second derivative wavelets obtained as linear combinations of cubic B-splines.

2.1.3 Filter Implementations

Since all two-dimensional filters used in the filter bank implementation of the transforms are x - y separable, only one-dimensional filters need to be implemented. We describe the implementation of finite impulse response (FIR) filters first and then treat prefiltering and postfiltering infinite impulse response (IIR) filters from Figure 3(a) and (b).

Let us refer to filters applied at scale 2^m as filters at level $m+1$, and let filters at level 1 (Equations (10), (14), (15), and (16) be called “original filters,” to distinguish them from their upsampled versions. Let us split the input to the filter bank from Figure 3 into image matrix rows and columns, each corresponding to a real signal $s(n) \in l^2(\mathbf{Z})$, $n \in [0, N-1]$. Depending on the length of each filter impulse response, filtering an input signal may be computed either by multiplying the discrete Fourier transforms of the two sequences or by circularly convolving $s(n)$ with a filter’s impulse response. Using circular rather than linear convolution, as is customary in image processing, can lead to boundary artifacts caused by

abrupt changes in the periodically extended signal. A common remedy for such a problem is realized by constructing a mirror extended signal [14]

$$s_{me}(n) = \begin{cases} s(-n-1) & \text{if } n \in [-N, -1] \\ s(n) & \text{if } n \in [0, N-1], \end{cases} \quad (19)$$

where we chose the signal $s_{me}(n)$ to be supported in $[-N, N-1]$.

Let us classify symmetric/antisymmetric real even-length signals into four types [15]:

Type I $f(n) = f(-n)$,

Type II $f(n) = f(-n-1)$,

Type III $f(n) = -f(-n)$,

Type IV $f(n) = -f(-n-1)$,

where $n \in [-N, N-1]$. Note that for Type I signals the values at $f(0)$ and $f(-N)$ are unique, and that for Type III signals the values at $f(0)$ and $f(-N)$ are equal to zero. (This is important for storage requirements: for signals of Type II or Type IV, N samples need to be saved, while Type I and Type III signals require $N+1$ and $N-1$ sample representations, respectively.)

Using properties of the Fourier transform, it is easy to show that the convolution of symmetric/antisymmetric real signals results in a symmetric/antisymmetric real signal. If a symmetric/antisymmetric real signal has an even length, then there always exists an integer shift such that the shifted signal belongs to one of the above types.

Now, we are ready to examine the filter bank implementation of the wavelet transform from Figure 3 with filters given by Equations (10), (14), (15), and (16) driven by mirrored signals of the form $s_{me}(n)$ from Equation (19) at the input. Let the number of levels M be restricted by

$$M \leq 1 + \log_2 \frac{N-1}{L_{max}-1}, \quad (20)$$

where L_{max} is the length of the longest original FIR filter impulse response.

Each FIR filter block in the filter bank consists of a filter and a circular shift operator.

Equation (20) guarantees that the length of the filter impulse response does not exceed the length of the signal at any block.

Since our mirror extended input row or column $s_{me}(n)$ is of Type II and noninteger shifts at level 1 are rounded to the nearest integer, it follows that a processed one-dimensional signal at any point in the filter bank belongs to one of the types defined above. This means that filtering a signal of length $2N$ can be reduced to filtering a signal of approximately one half of its length.

Implementation is particularly simple for FIR filters designed with $d=2$ and p odd. Filters are of Type I in this case, so their output will be of Type II. An FIR filter block from the filter bank shown in Figure 3 can therefore be implemented by

$$F_{s,m}u(n) = f(0)u_{II}(n) + \sum_{i=1}^{\frac{L-1}{2}} f(i)[u_{II}(n - 2^m i) + u_{II}(n + 2^m i)], \quad n \in [0, N-1], \quad (21)$$

where

$$u_{II}(n) = \begin{cases} u(-n-1) & \text{if } n \in [-\frac{N}{2}, -1] \\ u(n) & \text{if } n \in [0, N-1] \\ u(2N-n-1) & \text{if } n \in [N, \frac{3N}{2}] \end{cases} \quad (22)$$

$u(n)$ is an input signal to a block, $f(n)$ is an impulse response of $G^2(2^m\omega)$, $K^2(2^m\omega)$, $T(2^m\omega)$, or $H(2^m\omega)$ with p odd, L is the length of the filter, and N is the length of an input signal $s(n)$ to the filter bank. Implementation of filters $b_p(n)$ used for prefiltering and postfiltering (Figure 3(a) and (b)) represents a special case of Equation (21) with $m=0$. A filter bank with the above implementation of blocks and signal $s(n)$ at the input yields equivalent results as circular convolution of input $s_{me}(n)$ as defined by Equation (19). In addition to requiring one half the amount of memory, the computational savings over a circular convolution implementation of blocks are, depending on the original filter length, three to four times fewer multiplications and one half as many additions.

A similar approach is used for other filters. The problem becomes slightly more involved in this case, because the filters change type from first to subsequent levels, and the signal component type can be altered by a filter block as well. As a consequence, an implementation of blocks that use distinct original filters may not be the same, and the implementation of blocks at level 1 may differ from the implementation of blocks at other levels of analysis.

The decomposition blocks at level 1 can be implemented by

$$G_{-s,0}^1 u(n) = \sum_{i=0}^{\frac{L}{2}-1} g(i)[u_{II}(n-i-1) - u_{II}(n+i)], \quad n \in [1, N-1]$$

and

$$H_{-s,0} u(n) = \sum_{i=0}^{\frac{L}{2}-1} h(i)[u_{II}(n-i-1) + u_{II}(n+i)], \quad n \in [0, N],$$

for p even, where $u_{II}(l)$ is defined by (22), $g(n)$ and $h(n)$ are impulse responses of the filters computed from (10) and (16), respectively, and L is the length of the corresponding impulse response.

The output from a block $G_{-s}^1(\omega)$ at level 1 is of Type III, while the output from $H_{-s}(\omega)$ at the same level is of Type I.

The decomposition blocks at subsequent levels $m \in [1, M-1]$ can be implemented by

$$G_{-s,m}^1 u(n) = \sum_{i=0}^{\frac{L}{2}-1} g(i)[u_I(n - 2^m(i+s)) - u_I(n + 2^m(i+s))], \quad n \in [1, N-1],$$

for p even,

$$G_{-s,m}^1 u(n) = \sum_{i=0}^{\frac{L}{2}-1} g(i)[u_{II}(n - 2^m(i+s)) - u_{II}(n + 2^m(i+s))], \quad n \in [0, N-1],$$

for p odd,

$$F_{-s,m} u(n) = f(0)u_I(n) + \sum_{i=1}^{\frac{L}{2}-1} f(i)[u_I(n - 2^m i) + u_I(n + 2^m i)], \quad n \in [0, N], \quad (23)$$

with $f(n) = g(n)$ for $d=2$ and p even,

$$H_{-s,m} u(n) = \sum_{i=0}^{\frac{L}{2}-1} h(i)[u_I(n - 2^m(i+s)) + u_I(n + 2^m(i+s))], \quad n \in [0, N], \quad (24)$$

for p even, where

$$u_I(n) = \begin{cases} u(-n) & \text{if } n \in [-\frac{N}{2}, -1] \\ u(n) & \text{if } n \in [0, N] \\ u(2N - n) & \text{if } n \in [N+1, \frac{3N}{2}]. \end{cases} \quad (25)$$

The outputs from blocks $G_{-s}(2^m \omega)$ are of Type III for $d=1$ and p even, of Type IV for $d=1$ and p odd, and of Type I for $d=2$ and p even, whereas the outputs from $H_{-s}(2^m \omega)$ are of Type I for p even.

Next, the reconstruction blocks at level 1 can be implemented by

$$K_{s,0}^1 u(n) = \sum_{i=1}^{\frac{L}{2}} k(i)[u_{III}(n - i + 1) - u_{III}(n + i)], \quad n \in [0, N-1]$$

and

$$H_{s,0} u(n) = \sum_{i=1}^{\frac{L}{2}} h(i)[u_I(n - i + 1) + u_I(n + i)], \quad n \in [0, N-1],$$

for p even, where

$$u_{III}(n) = \begin{cases} -u(-n) & \text{if } n \in [-\frac{N}{2}, -1] \\ 0 & \text{if } n = 0 \\ u(n) & \text{if } n \in [1, N-1] \\ 0 & \text{if } n = N \\ -u(2N - n) & \text{if } n \in [N+1, \frac{3N}{2}], \end{cases} \quad (26)$$

$u_I(n)$ is as defined by (25) and $k(n)$ is an impulse response of the filter from (14). Note that both outputs from blocks $K_s^1(\omega)$ and $H_s(\omega)$ are of Type II.

The reconstruction blocks at subsequent levels can be implemented by

$$K_{s,m}^d u(n) = \sum_{i=0}^{\frac{L}{2}-1} k(i+1)[u_{III}(n - 2^m(i+s)) - u_{III}(n + 2^m(i+s))], \quad n \in [0, N],$$

for $d=1$ and p even, (23) with $f(n) = k(n)$ for $d=2$ and p even,

$$K_{s,m}^d u(n) = \sum_{i=0}^{\frac{L}{2}-1} k(i+1)[u_{IV}(n - 2^m(i+s)) - u_{IV}(n + 2^m(i+s))], \quad n \in [0, N-1],$$

for $d=1$ and p odd,

$$H_{s,m} u(n) = H_{-s,m} u(n),$$

for p even, where $u_{III}(l)$ is given by (26),

$$u_{IV}(n) = \begin{cases} -u(-n-1) & \text{if } n \in [-\frac{N}{2}, -1] \\ u(n) & \text{if } n \in [0, N-1] \\ -u(2N-n-1) & \text{if } n \in [N, \frac{3N}{2}], \end{cases}$$

and $H_{-s,m} u(n)$ is specified by Equation (24). We observe that the outputs from blocks $K_s^d(2^m\omega)$ and $H_s(2^m\omega)$, $m \in [1, M-1]$, for p even are of Type I.

When we compare the above implementation of blocks to circular convolution driven by a mirrored signal $s_{me}(n)$ at the input, we observe that approximately twofold less memory space, three to four times fewer multiplications and one half as many additions are required. (For Type I signals an additional sample has to be stored because two values are without a pair).

The implementation presented in this section performs all operations in the spatial domain; however, one could also implement the structures shown in Figure 3 with an input signal $s_{me}(n)$ in the frequency domain. For short filter impulse responses, such as those given in Tables 3, 4 and 5, the spatial implementation described in this section is certainly more efficient. For long filter impulse responses, however, filtering is faster if implemented in the frequency domain. Additional details on alternative FIR filter implementation strategies can be found in [16].

Implementation of IIR filters $b_p^{-1}(n)$ used for prefiltering and postfiltering is a bit more involved than the one of their FIR counterparts. Fortunately, the number of different cases is much smaller here: possible input to $b_p^{-1}(n)$ in the filter bank from Figure 3 is either of Type II or of Type I (symmetry types for IIR filters slightly differ from those defined for FIR filters: here, mirror extended signals are periodically repeated, so that they stretch from $-\infty$ to ∞). We use ideas and a few results from [17].

Let us first take a closer look at the system function $B_p^{-1}(z)$ with $p \in \{2, 3\}$. This function can be written as a cascade of terms

$$E(z) = \frac{1}{z - \frac{1+\alpha^2}{\alpha} + z^{-1}} = \frac{-\alpha}{(1 - \alpha z^{-1})(1 - \alpha z)}, \quad (27)$$

which can be expressed in a parallel form as

$$E(z) = \frac{-\alpha}{1 - \alpha^2} \left(\frac{1}{1 - \alpha z^{-1}} + \frac{1}{1 - \alpha z} - 1 \right), \quad (28)$$

where α and $\frac{1}{\alpha}$ are poles of the causal and the anticausal filter, respectively.

The impulse response of this term can be written as

$$e(n) = \frac{-\alpha}{1 - \alpha^2} \alpha^{|n|}.$$

We choose to implement $E(z)$ in a cascade form and therefore extract the difference equations from Equation (27):

$$c^+(n) = u(n) + \alpha c^+(n-1) \quad n = 1, 2, \dots, N-1, \quad (29)$$

and

$$c(n) = \alpha (c(n+1) - c^+(n)) \quad n = N-2, N-3, \dots, 0, \quad (30)$$

where $u(n)$ denotes the input to the block, $c^+(n)$ is the output from the causal part, and $c(n)$ stands for the output from the block.

To solve Equations (29) and (30) we need boundary conditions $c^+(0)$ and $c(N-1)$. We derive

$$c^+(0) = \sum_{i=-\infty}^0 \alpha^{-i} u_{IIp}(i) = u(0) + \sum_{i=0}^{N-1} \frac{\alpha^{i+1} + \alpha^{2N-i}}{1 - \alpha^{2N}} u(i) \simeq u(0) + \sum_{i=0}^{i_0} \alpha^{i+1} u(i), \quad (31)$$

and, using parallel form (28)

$$\begin{aligned} c(N-1) &= \frac{-\alpha}{1 - \alpha^2} (c^+(N-1) + \sum_{i=0}^{N-1} \frac{\alpha^{N-i} + \alpha^{N+1+i}}{1 - \alpha^{2N}} u(i)) \simeq \\ &\simeq \frac{-\alpha}{1 - \alpha^2} (c^+(N-1) + \sum_{i=N-1-i_0}^{N-1} \alpha^{N-i} u(i)), \end{aligned} \quad (32)$$

where

$$\begin{aligned} u_{IIp}(n) &= \begin{cases} u_{II}(n \bmod (2N)) & \text{if } n \geq 0 \\ u_{II}(-(n+1) \bmod (2N)) & \text{if } n < 0, \end{cases} \\ u_{II}(n) &= \begin{cases} u(n) & \text{if } n \in [0, N-1] \\ u(2N-n-1) & \text{if } n \in [N, 2N-1], \end{cases} \end{aligned}$$

N is the length of an input signal to the filter bank, and $i_0 < N-1$ is selected such that α^{i_0} falls below a predefined precision threshold.

For orders p greater than three, we implement $B_p^{-1}(z)$ as a cascade of terms $E(z)$ with different α 's. Note that the output from block $E(z)$ is always of the same type as the input to it.

2.2 Image Fusion

Image fusion combines particular aspects of information from the same imaging modality or from distinct imaging modalities and can be used to improve the reliability of a particular computational vision task or to provide a human observer with a deeper insight about the nature of observed data. Whether it is combining different sensors or extending the dynamic range of a single sensor, the goal is to achieve more accurate inferences that can be achieved by a single sensor or a single sensor setting. By fusing together processed sections of images, a combined image which is superior to the sum of its parts can be constructed. The simplest method of fusing images is accomplished by computing their average. Such a technique does combine features from input images in the fused image, however, the contrast of the original features can be significantly reduced. Among more sophisticated methods, multiscale and multiresolution analyses have become particularly popular. Different pyramids [18, 19] and wavelet-based techniques [20, 21, 22, 23] have been applied to this problem.

In Section 2.2.1, we compared an image fusion method based upon the steerable dyadic wavelet transform with recently published fusion methods based upon the gradient pyramid, the orthogonal wavelet transform, and the biorthogonal wavelet transform. Section 2.2.2 then presents an application of the fusion mechanism to the problem of mammographic feature contrast enhancement.

2.2.1 Comparison of Transforms

Gradient Pyramid

Gaussian pyramid [4] was used for construction of a gradient pyramid used in [18]. Let the generating filter kernel for the Gaussian pyramid be

$$w(n_x, n_y) = w_b * w_b(n_x, n_y) = \frac{1}{256} \begin{bmatrix} 1 & 4 & 6 & 4 & 1 \\ 4 & 16 & 24 & 16 & 4 \\ 6 & 24 & 36 & 24 & 6 \\ 4 & 16 & 24 & 16 & 4 \\ 1 & 4 & 6 & 4 & 1 \end{bmatrix},$$

where $w_b(n_x, n_y)$ denotes the 3×3 binomial filter:

$$w_b(n_x, n_y) = \frac{1}{16} \begin{bmatrix} 1 & 2 & 1 \\ 2 & 4 & 2 \\ 1 & 2 & 1 \end{bmatrix}.$$

Level $m \in \mathbf{N}$ of the Gaussian pyramid for an input image matrix $s(n_x, n_y)$ is then

$$\mathcal{G}_m s(n_x, n_y) = (w * \mathcal{G}_{m-1} s(n_x, n_y))_{\downarrow 2},$$

with

$$\mathcal{G}_0 s(n_x, n_y) = s(n_x, n_y).$$

Gradient pyramid is obtained from the Gaussian pyramid as

$$\mathcal{D}_m^i s(n_x, n_y) = d_i * (\mathcal{G}_m s(n_x, n_y) + w_b * \mathcal{G}_m s(n_x, n_y)),$$

where

$$\begin{aligned} d_1 &= \begin{bmatrix} 1 & -1 \end{bmatrix}, \\ d_2 &= \frac{1}{\sqrt{2}} \begin{bmatrix} 0 & -1 \\ 1 & 0 \end{bmatrix}, \\ d_3 &= \begin{bmatrix} -1 \\ 1 \end{bmatrix}, \text{ and} \\ d_4 &= \frac{1}{\sqrt{2}} \begin{bmatrix} -1 & 0 \\ 0 & 1 \end{bmatrix}. \end{aligned}$$

An image is reconstructed from the gradient pyramid by converting the pyramid to the Laplacian and then to the Gaussian pyramid. The Laplacian pyramid is approximated as

$$\widehat{\mathcal{L}}_m s(n_x, n_y) \simeq \mathcal{K}_m s(n_x, n_y) + w * \mathcal{K}_m s(n_x, n_y), \quad (33)$$

where

$$\mathcal{K}_m s(n_x, n_y) = -\frac{1}{8} \sum_{i=1}^4 d_i * \mathcal{D}_m^i s(n_x, n_y).$$

An approximation to the Gaussian pyramid is obtained by

$$\widehat{\mathcal{G}}_m s(n_x, n_y) = \widehat{\mathcal{L}}_m s(n_x, n_y) + 4w * (\widehat{\mathcal{G}}_{m+1} s(n_x, n_y))_{\uparrow 2}.$$

Note that, since the filters d_i have the center of symmetry between samples, they need to be shifted for reconstruction, and that, because of the approximation (33), the gradient pyramid does not have the perfect reconstruction property.

Discrete Wavelet Transform

Discrete wavelet transform was implemented as a perfect reconstruction filter bank [24]. In two dimensions, the transform is obtained by applying the one-dimensional transform separately along each dimension. Level $m \in N$ of the transformed image matrix $s(n_x, n_y)$ is therefore

$$\begin{aligned}\mathcal{W}_m^d s(n_x, n_y) &= ((\mathcal{A}_{m-1} s(n_x, n_y) * \tilde{g}(n_x))_{\downarrow 2} * \tilde{g}(n_y))_{\downarrow 2}, \\ \mathcal{W}_m^v s(n_x, n_y) &= ((\mathcal{A}_{m-1} s(n_x, n_y) * \tilde{g}(n_x))_{\downarrow 2} * \tilde{h}(n_y))_{\downarrow 2}, \\ \mathcal{W}_m^h s(n_x, n_y) &= ((\mathcal{A}_{m-1} s(n_x, n_y) * \tilde{h}(n_x))_{\downarrow 2} * \tilde{g}(n_y))_{\downarrow 2}, \text{ and} \\ \mathcal{A}_m s(n_x, n_y) &= ((\mathcal{A}_{m-1} s(n_x, n_y) * \tilde{h}(n_x))_{\downarrow 2} * \tilde{h}(n_y))_{\downarrow 2},\end{aligned}$$

where

$$\mathcal{A}_0 s(n_x, n_y) = s(n_x, n_y), \quad (34)$$

$\{\mathcal{W}_m^d s(n_x, n_y), \mathcal{W}_m^v s(n_x, n_y), \mathcal{W}_m^h s(n_x, n_y)\}_{m \in [1, M]}$ and $\mathcal{A}_M s(n_x, n_y)$ are detail and approximation coefficients for M levels of analysis, respectively, and $\tilde{g}(n)$ and $\tilde{h}(n)$ are the decomposition filters.

Reconstruction of the approximation coefficients at the previous level is given by

$$\begin{aligned}\mathcal{A}_{m-1} s(n_x, n_y) &= ((\mathcal{W}_m^d s(n_x, n_y))_{\uparrow 2} * \bar{g}(n_y) + (\mathcal{W}_m^v s(n_x, n_y))_{\uparrow 2} * \bar{h}(n_y))_{\uparrow 2} * \bar{g}(n_x) + \\ &+ ((\mathcal{W}_m^h s(n_x, n_y))_{\uparrow 2} * \bar{g}(n_y) + (\mathcal{A}_m s(n_x, n_y))_{\uparrow 2} * \bar{h}(n_y))_{\uparrow 2} * \bar{h}(n_x),\end{aligned}$$

with $\bar{g}(n)$ and $\bar{h}(n)$ being the reconstruction filters.

Two-dimensional wavelets associated with separable filter banks, such as the one just described, were constructed from tensor products of two one-dimensional multiresolution analyses (wavelets are products of one-dimensional wavelets and scaling functions) [6]. Note also that, due to oversimplified initialization (34), the discrete wavelet transform may be a pretty poor approximation to samples of the continuous wavelet transform.

We limited ourselves to FIR filters (i.e., compactly supported wavelets). In our experiments, we used orthogonal wavelet transform with DAUB12 wavelet [6], and biorthogonal wavelet transform with Bior6.8 wavelet from MATLAB Wavelet Toolbox. Image fusion is performed in the transform space by computing local statistics across the decomposition scales, and reconstructing from fused transform coefficients. Typical size of neighborhood is between a single pixel and 5×5 area with some loss of contrast reported for the latter [18]. In general, the chosen size of the area represents a tradeoff between sharpness and introduction of artifacts. In order to achieve our goal of maximum contrast with minimum artifacts, we limit the neighborhood to a single pixel (maximizing contrast) and try to choose the most appropriate transform (minimizing artifacts).

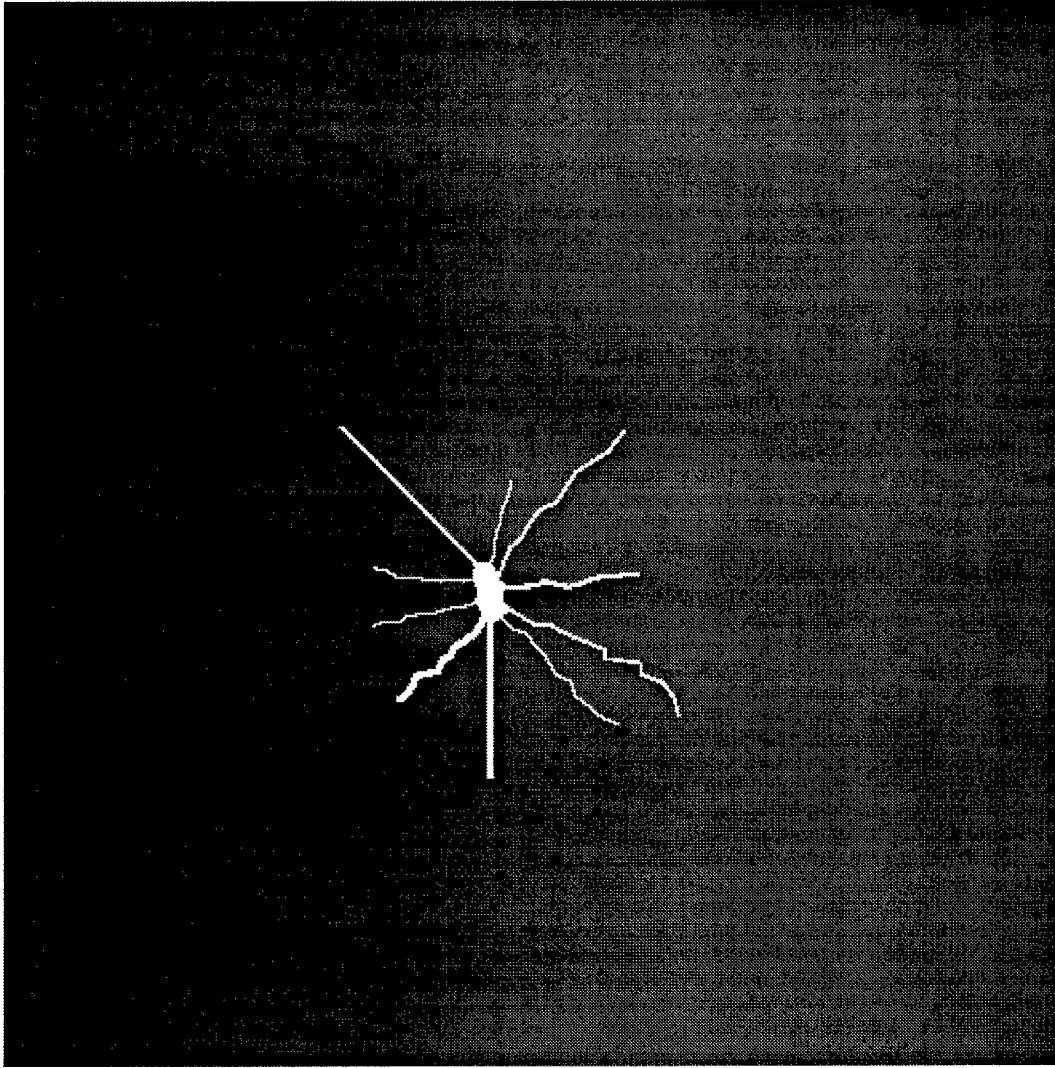


Figure 5: Phantom used for comparisons of different transforms for image fusion.

After the transform decompositions of images to be fused is performed, the corresponding transform coefficients of the images are combined according to the fusion rule into a new set of transform coefficients from which the fused result is reconstructed. As a fusion rule, we used the maximum magnitude rule (at each position and scale of the transforms the coefficient with greatest magnitude is chosen) for the gradient pyramid, the orthogonal wavelet transform (DAUB12), and the biorthogonal wavelet transform (Bior6.8), and the maximum oriented energy rule (at each position and scale of the transforms the coefficient with greatest local oriented energy is selected) for steerable wavelet transform [21]. Our first two experiments used the phantom shown in Figure 5. Image matrix has dimensions 512×512 , and fusion was performed between the original and shifted phantom. First, the image to be fused with the one from Figure 5 was generated by shifting the

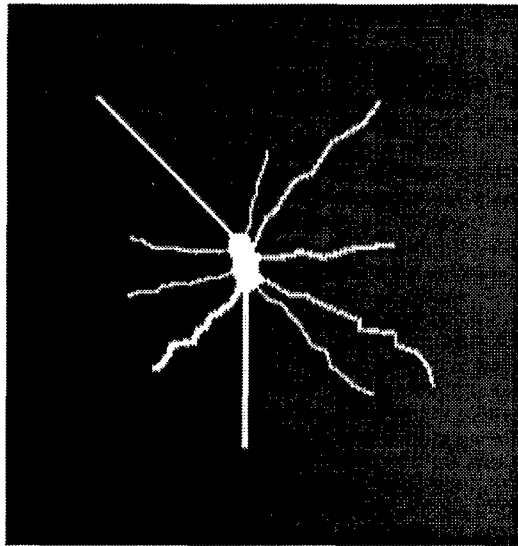
Table 6: Performance of fusion algorithms based on four different transforms.

Transform	MSE	MAE
Gradient pyramid	28.66	13
Orthogonal WT	0.14	8
Biorthogonal WT	0.21	7
Steerable WT	0.05	6

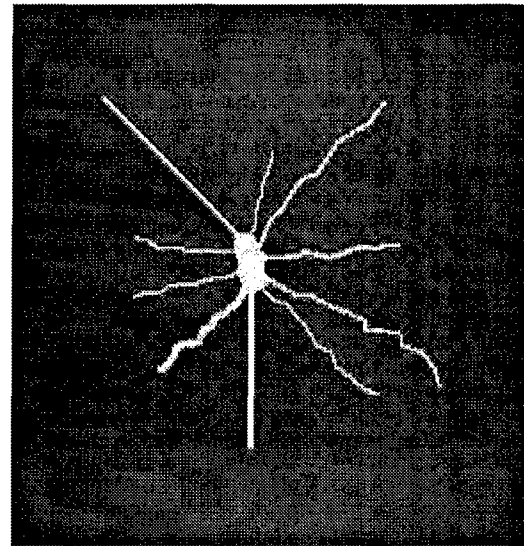
phantom one sample vertically towards the top of the image. The ideal result of fusion should contain no double lines or other artifacts (the distance between the corresponding points in two images is one pixel, so that the algorithm should merge shifted features into a single feature). Figure 6 shows the phantom with the surrounding area in the fused images. The resulting images from all four transforms were clipped (pixel values above the upper limit of the gray level range were mapped to white) rather than scaled. Please note the artifacts present when the orthogonal and biorthogonal wavelet transforms were used. The latter produced a slightly better result, although artifacts due to aliasing and tensor product representation made both fused images unacceptable.

Our second experiment differed from the first one only in the fact that the phantom from Figure 5 was shifted by five samples. Here, the shift is large enough that features from both images may be present in the fused image. The phantom with its surroundings in the results of fusion using the four transforms is demonstrated in Figure 7. Please note that the situation is similar to the one in the first experiment. Both orthogonal and biorthogonal wavelet transforms exhibited obvious artifacts, while the redundant gradient pyramid and steerable dyadic wavelet transform performed well.

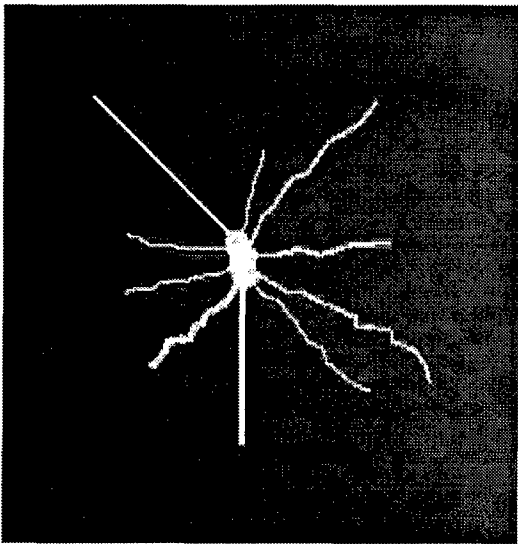
The third experiment was geared towards a quantitative comparison of the four transforms for image fusion. Similar to [22], we blur different parts of the image and then fuse them in such a way that each blurred part is fused with its original counterpart. The ideal result of fusion would be the original image. Figure 8 shows the original 512×512 mammogram, 100×100 area of interest, and two blurred images to be fused. Mean-square error (MSE) and maximum absolute error (MAE) between the result of fusion and the original image were computed for all four methods. Table 6 summarizes the results. Let us remark that these results are rather typical; on a variety of images, wavelet based methods were very close, while consistently outperforming the gradient pyramid according to the two criteria. No significant artifacts were noticed in the “blurring experiments.” By comparing the extracted regions with the original ones, we subjectively rated the transforms used for fusion as: (1) steerable dyadic wavelet transform, (2) biorthogonal wavelet transform, (3) orthogonal wavelet transform, and (4) gradient pyramid. Again, the differences between different types of wavelet transforms were minor, whereas the gradient pyramid lagged



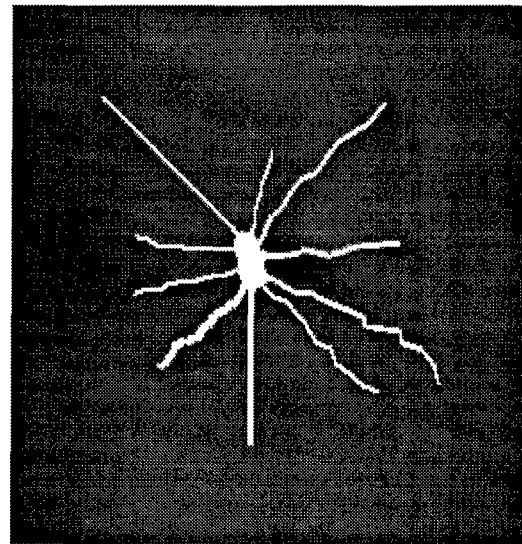
(a)



(b)

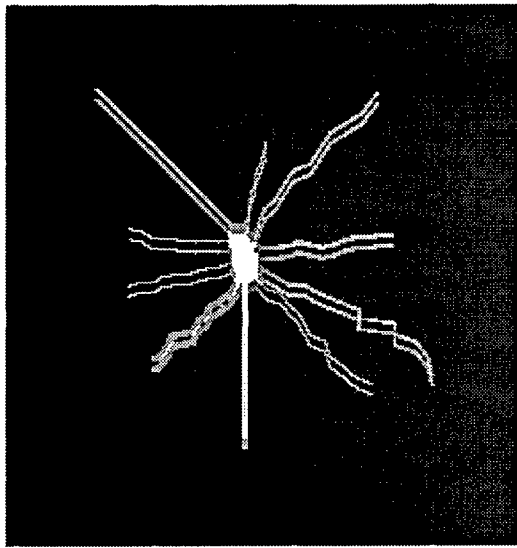


(c)

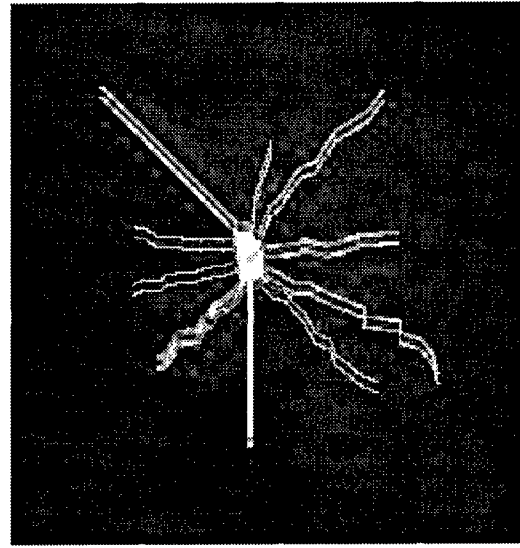


(d)

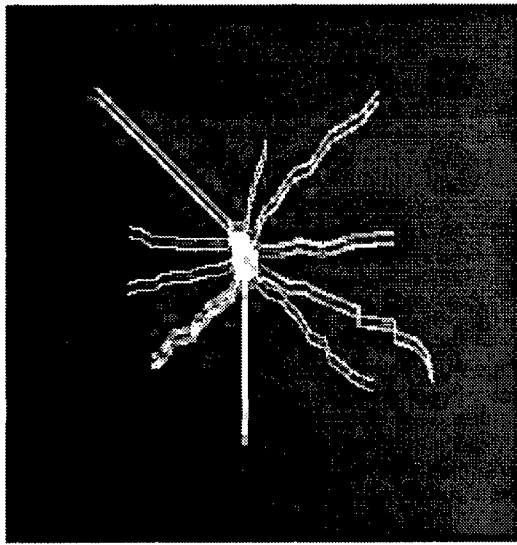
Figure 6: Image fusion of phantoms shifted by one sample. (a) Gradient pyramid. (b) Orthogonal wavelet transform. (c) Biorthogonal wavelet transform. (d) Steerable dyadic wavelet transform.



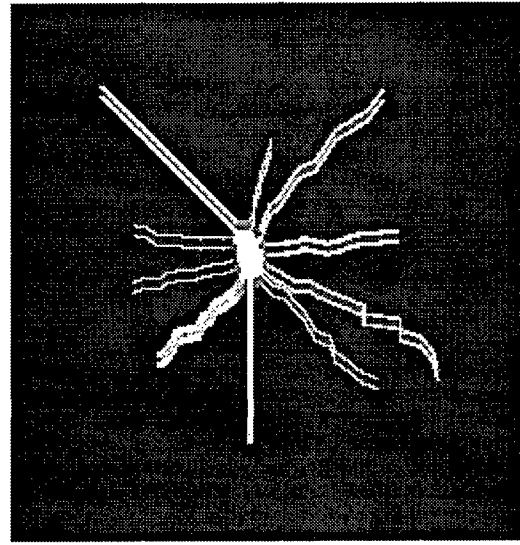
(a)



(b)

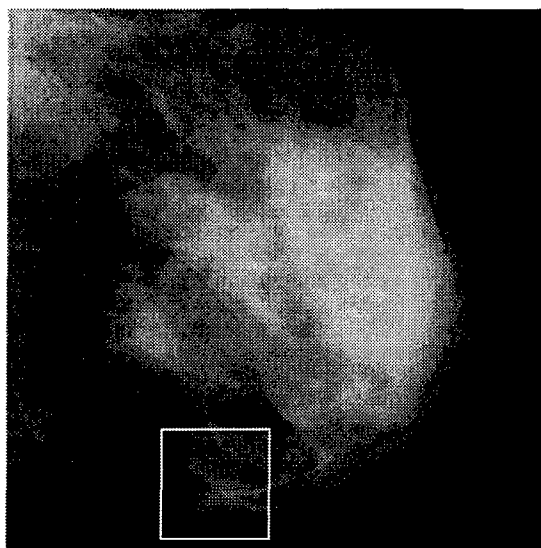


(c)

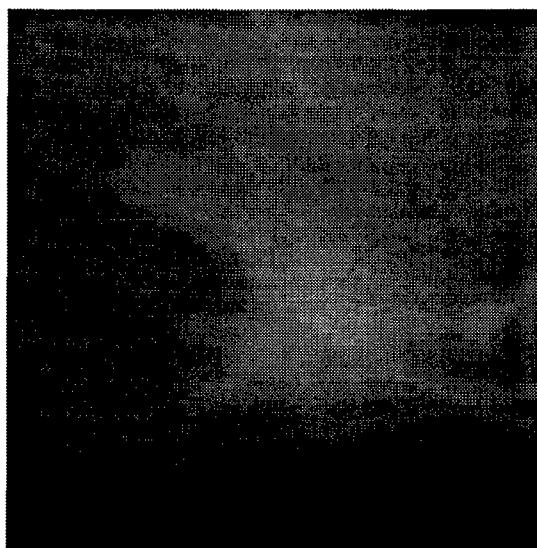


(d)

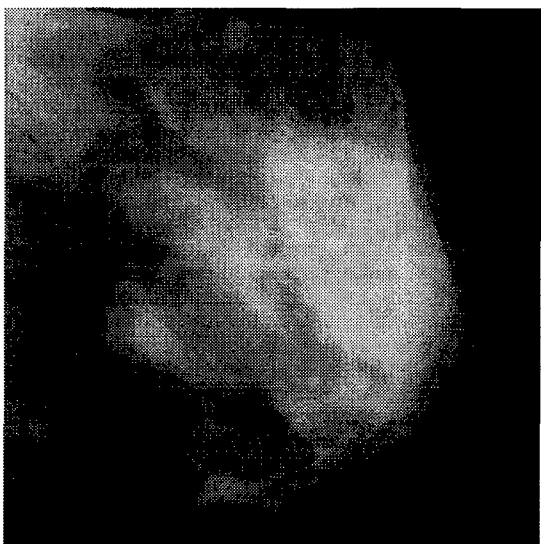
Figure 7: Image fusion of phantoms shifted by five samples. (a) Gradient pyramid. (b) Orthogonal wavelet transform. (c) Biorthogonal wavelet transform. (d) Steerable dyadic wavelet transform.



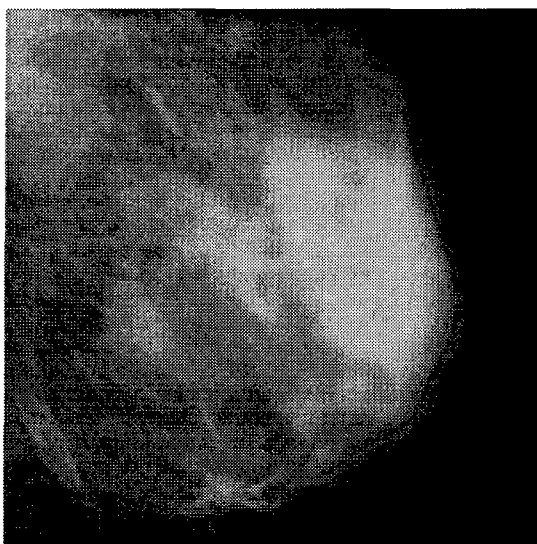
(a)



(b)



(c)



(d)

Figure 8: (a) Mammogram with area of interest delineated. (b) Area of interest. (c) Image from (a) with left half blurred. (d) Image from (a) with right half blurred.

behind. Regions of interest corresponding to the one from Figure 8(b) are shown in Figure 9. Wavelet based methods produced results that are visually close to the original region, gradient pyramid, however, caused loss of sharpness.

2.2.2 Fusion of Enhanced Features

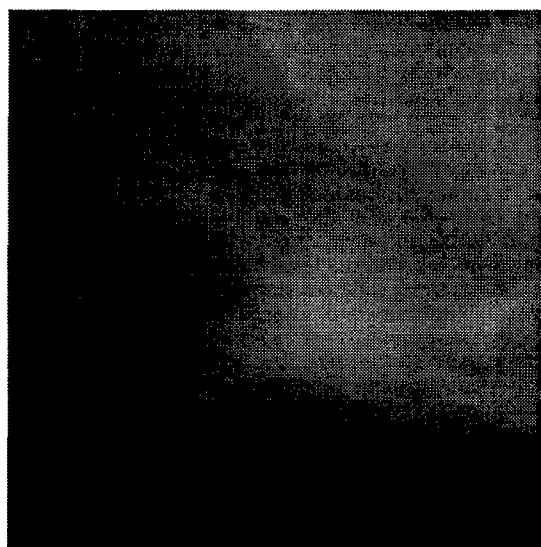
Existing methods of mammographic image enhancement can be divided roughly into two categories: (1) methods aimed at better visualization of all features present in the image [25, 26, 27, 28], and (2) methods that target specific features of importance (e.g., microcalcifications [29, 30], stellate lesions [11]).

Methods from the first category are not optimized for a specific type of cancer and frequently not even for mammography. Rather, they try to improve the perceptual quality of the entire image and are often developed with a framework more general than mammography alone in mind.

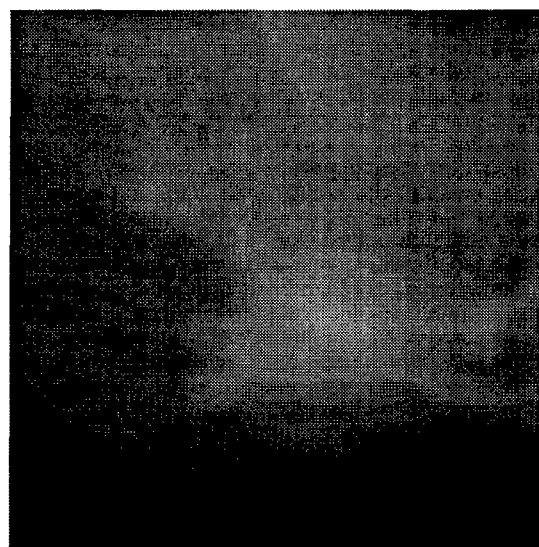
The second category methods concentrate on revelation of particular signs of malignancy. They can be very successful in their area of specialization; however, in order to process mammogram for presence of various features, one would need to apply different algorithms independently resulting in both larger number of images to be interpreted by a radiologist and increased computational complexity of such a procedure.

Here, we present an approach which overcomes these shortcomings and problematic limitations via synthesis of the two paradigms by means of image fusion.

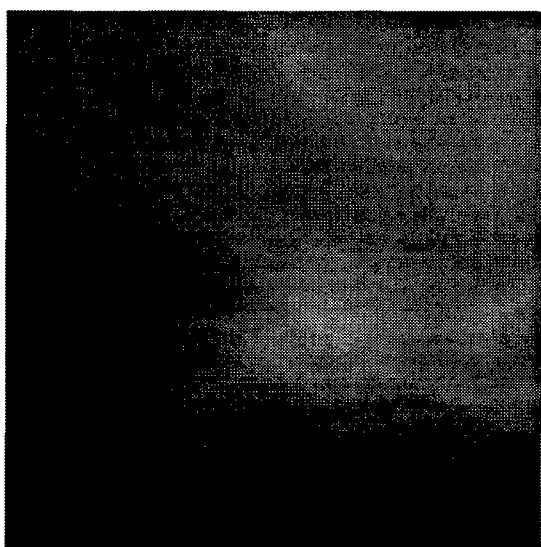
The goal of our method is to adapt specific enhancement schemes for distinct mammographic features, and then combine the set of processed images into an enhanced image. The input mammographic image is first processed for enhancement of microcalcifications, masses, and stellate lesions. From the resulting enhanced images, the final enhanced image is synthesized by means of image fusion. Wavelet based image enhancement and fusion are merged into a unified framework, so that there is no need for carrying out the two operations independently (i.e., computing wavelet decompositions, modifying wavelet coefficients for enhancement of specific features, reconstructing the enhanced images, performing wavelet transforms of the enhanced images, fusing transform coefficients, and obtaining the final result by reconstruction from fused wavelet coefficients). Both enhancement and fusion are therefore implicit (i.e., performed in the wavelet domain only). Figure 10 presents a block scheme of the overall algorithm. The algorithm consists of two major steps: (1) wavelet coefficients are modified distinctly for each type of malignancy; (2) the obtained multiple sets of wavelet coefficients are fused into a single set from which the reconstruction is computed. The devised scheme allows efficient deployment of an enhancement strategy appropriate for clinical screening



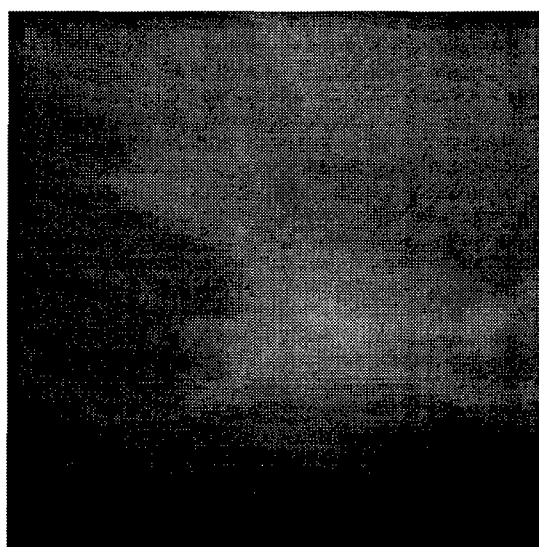
(a)



(b)



(c)



(d)

Figure 9: Region of interest corresponding to the one from Figure 8(b) extracted from the fused images using: (a) gradient pyramid, (b) orthogonal wavelet transform, (c) biorthogonal wavelet transform, and (d) steerable dyadic wavelet transform.

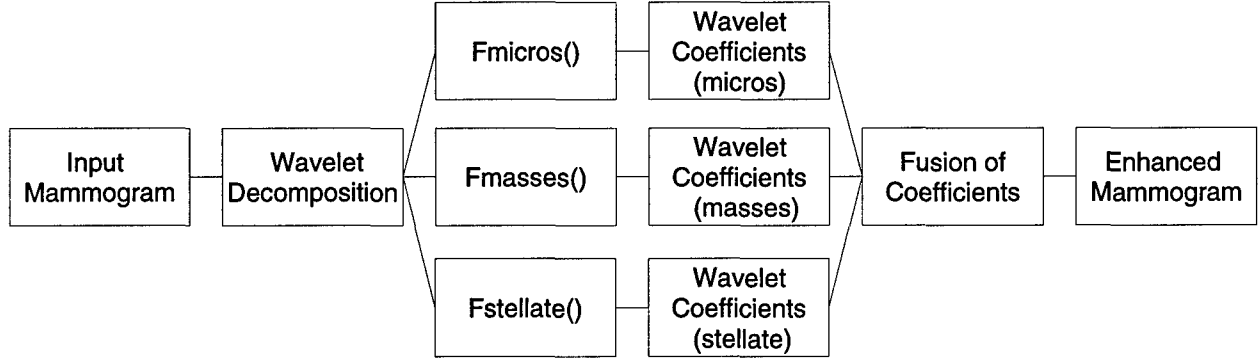


Figure 10: Overview of the algorithm.

protocols: enhancement algorithm is first developed for each specific type of feature independently, and the results are then combined using an appropriate fusion strategy. The structure of the algorithm also enables independent development and optimization of enhancement strategies for individual mammographic features as well as the fusion module.

Microcalcifications

Microcalcifications appear on mammograms in approximately half of breast cancer cases. The assessment of shape, number, and distribution of microcalcifications is important for a radiologist to reach the correct diagnosis. Microcalcifications are smaller than 1 mm in size and can be difficult to locate when they are superimposed on dense breast tissue. Several techniques have been developed to improve the visibility of microcalcifications [29, 30, 31, 32]. The approach devised by Strickland and Hahn [29] is particularly well suited for our framework: they used an undecimated wavelet transform to approximate second derivatives of a Gaussian probability density function for a multiscale matched filtering for presence of microcalcifications.

Strickland and Hahn based their method on the observation that the average microcalcification can be modeled by a circularly symmetric Gaussian function. Using a combination of a separable Markov process with autocorrelation $r_{nn} = \sigma_n^2 e^{-\alpha\sqrt{|k|+|l|}}$ and a nonseparable Markov process with autocorrelation $r_{nn} = \sigma_n^2 e^{-\alpha\sqrt{k^2+l^2}}$ to represent mammogram texture, they obtained the separable matched filter

$$M_{sep}(\omega_x, \omega_y) = M(\omega_x)M(\omega_y), \quad (35)$$

where

$$M(\omega) \simeq \frac{\sigma\sqrt{\pi}\omega^2}{\sqrt{2\alpha}\sigma_n} e^{\frac{\sigma^2\omega^2}{2}},$$

and the nonseparable matched filter

$$M_{nsep}(\omega_x, \omega_y) \simeq \frac{\pi\sigma^2}{\sigma_n^2} (\omega_x^2 + \omega_y^2) e^{\frac{\sigma^2\omega^2}{2}}. \quad (36)$$

In order to deal with different sizes of microcalcifications, one must vary σ of matched filters (35) and (36) appropriately. In Strickland and Hahn's scheme, a wavelet decomposition was chosen to approximate the matched filters across the desired scale range. Considering the $100\mu\text{m}$ resolution of the Nijmegen database, the wavelet transform was computed over the first 4 octaves. For a denser sampling of scale, voices were inserted at octaves "2.5" and "3.5." The wavelet analysis stage acted as a bank of matched filters; wavelet coefficients at locations indicating microcalcifications were multiplied by a gain factor, and then the inverse wavelet transform was applied to the modified coefficients. In our approach, microcalcifications are modeled by central B-splines. Using the relation between the standard deviation of a Gaussian function and the order of B-splines that approximate it $\sigma = \sqrt{\frac{p+1}{12}}$ [33], the assumption that a Gaussian object is visible approximately over $\pm\sigma$ pixels [29], and the fact that the mammograms in the University of Florida database were digitized at $116\mu\text{m}$ resolution, four levels of the transform from Section 2.1 with, for example, $p=3$ are needed to encompass different sizes of microcalcifications. The wavelet decomposition including voices at scales 3 and 6 (corresponding to Strickland and Hahn's octaves "2.5" and "3.5") can be obtained by deriving a counterpart to Equation (18) for the two scales.

$\hat{\beta}_p(3\omega)$ can be related to $\hat{\beta}_p(\omega)$ by expressing $\hat{\beta}_p(3\omega)$ as (cf. Proposition 1 of [34])

$$\hat{\beta}_p(3\omega) = \frac{1}{3^{p+1}} \left(\frac{\sin\left(\frac{3\omega}{2}\right)}{\sin\left(\frac{\omega}{2}\right)} \right)^{p+1} \left(\frac{\sin\left(\frac{\omega}{2}\right)}{\frac{\omega}{2}} \right)^{p+1}.$$

Using $\sum_{m=0}^M e^{j(m\omega+\theta)} = \frac{\sin\left(\frac{(M+1)\omega}{2}\right)}{\sin\left(\frac{\omega}{2}\right)} e^{j\left(\frac{M\omega}{2}+\theta\right)}$, we get

$$\hat{\beta}_p(3\omega) = V(\omega) \hat{\beta}_p(\omega),$$

where

$$V(\omega) = \left(\frac{1}{3} (e^{-j\omega} + 1 + e^{j\omega}) \right)^{p+1}.$$

Filter $V(\omega)$ can be implemented as a moving sum with $2(p+1)$ additions per sample and a multiplicative factor $\frac{1}{3^{p+1}}$ applied to the wavelet coefficients [34].

Next, $\hat{\beta}_p(6\omega)$ is expressed by means of Equation (17):

$$\hat{\beta}_p(6\omega) = H_{-s}(3\omega) \hat{\beta}_p(3\omega)$$

with odd orders p used for the sampling shift s to be zero.

Now, we can write

$$\begin{aligned} \mathcal{F}\{W_3^i s(x, y) \big|_{x=n_x, y=n_y}\} &\simeq S(\omega_x, \omega_y) B_r^{-1}(\omega_x) B_r^{-1}(\omega_y) B_{p+r+i+1}(\omega_x) \cdot \\ &\cdot B_{p+r+d-i+1}(\omega_y) G_{-s}^{d-i}(3\omega_x) G_{-s}^i(3\omega_y) V^{p+i}(\omega_x) V^{p+d-i}(\omega_y) \end{aligned} \quad (37)$$

and

$$\begin{aligned} \mathcal{F}\{W_6^i s(x, y) \big|_{x=n_x, y=n_y}\} &\simeq S(\omega_x, \omega_y) B_r^{-1}(\omega_x) B_r^{-1}(\omega_y) B_{p+r+i+1}(\omega_x) \cdot \\ &\cdot B_{p+r+d-i+1}(\omega_y) G_{-s}^{d-i}(6\omega_x) G_{-s}^i(6\omega_y) H_{-s}^{p+i}(3\omega_x) H_{-s}^{p+d-i}(3\omega_y) V^{p+i}(\omega_x) V^{p+d-i}(\omega_y) \end{aligned} \quad (38)$$

with notation being the same as in Equation (18), and superscript p in $H_{-s}^p(\omega)$ denoting the order p in Equation (16).

Wavelet coefficients obtained via Equations (37) and (38) are not used for reconstruction—the inverse transform is carried out as given in Section 2.1.

The decomposition described by Equations (18), (37), and (38) with additional filtering by $G^2(l\omega)$ at each scale $l \in \{1, 2, 3, 4, 6, 8\}$ enables approximations to the second derivatives of Gaussian along both x and y directions and to Laplacian of Gaussian across distinct scales employed by Strickland and Hahn [29] (cf. Equations (35) and (36)). We proceed in a similar fashion as therein: the two outputs per scale are thresholded independently, all binary results are then combined, a circular region centered at detected pixel locations are next multiplied by a gain, and, finally, the reconstruction process uses modified transform coefficients.

Circumscribed Masses

Almost half of missed cancers appear on mammograms as masses. Perception is a problem particularly for patients with dense fibroglandular patterns. The detection of masses can be especially difficult because of their small size and subtle contrast compared with normal breast structures.

Fan and Laine [26] developed a discrete dyadic wavelet transform based algorithm suitable for enhancement of masses. They constructed an approximation to Laplacian of Gaussian across dyadic scales for an isotropic input to a piecewise linear enhancement function.

Approximation to Laplacian of Gaussian across dyadic scales is easy to obtain using multiscale spline derivatives derived in Section 2.1: Equation (18) with $i=0$ and $i=2$ approximates the second derivative of a Gaussian function along directions of x and y axis, respectively (the corresponding branches in Figure 3(c) are the first and third from the top). The appropriate transform coefficient at each dyadic scales are therefore added and

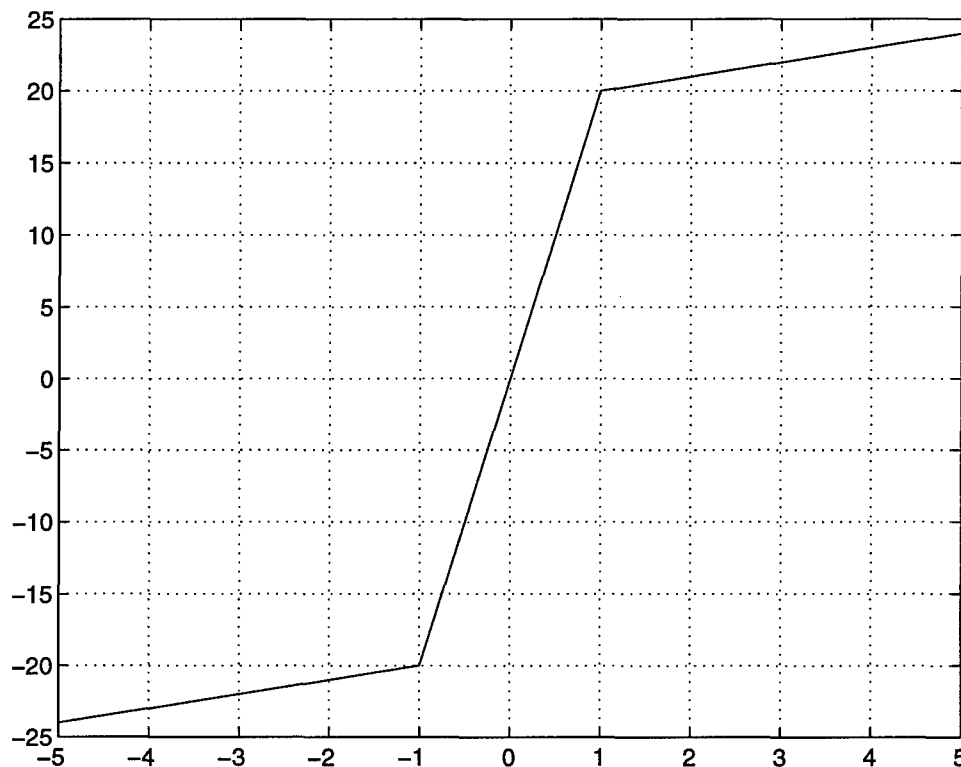


Figure 11: Enhancement function (Equation (39) with $K = 20$ and $T = 1$).

their sum input to the piecewise linear function

$$C(x) = \begin{cases} x - (K-1)T & \text{if } x < -T \\ Kx & \text{if } |x| \leq T \\ x + (K-1)T & \text{if } x > T. \end{cases} \quad (39)$$

used at each level $m+1$ of the transform separately. Due to the expected size of masses, levels greater than 4 are enhanced more aggressively.

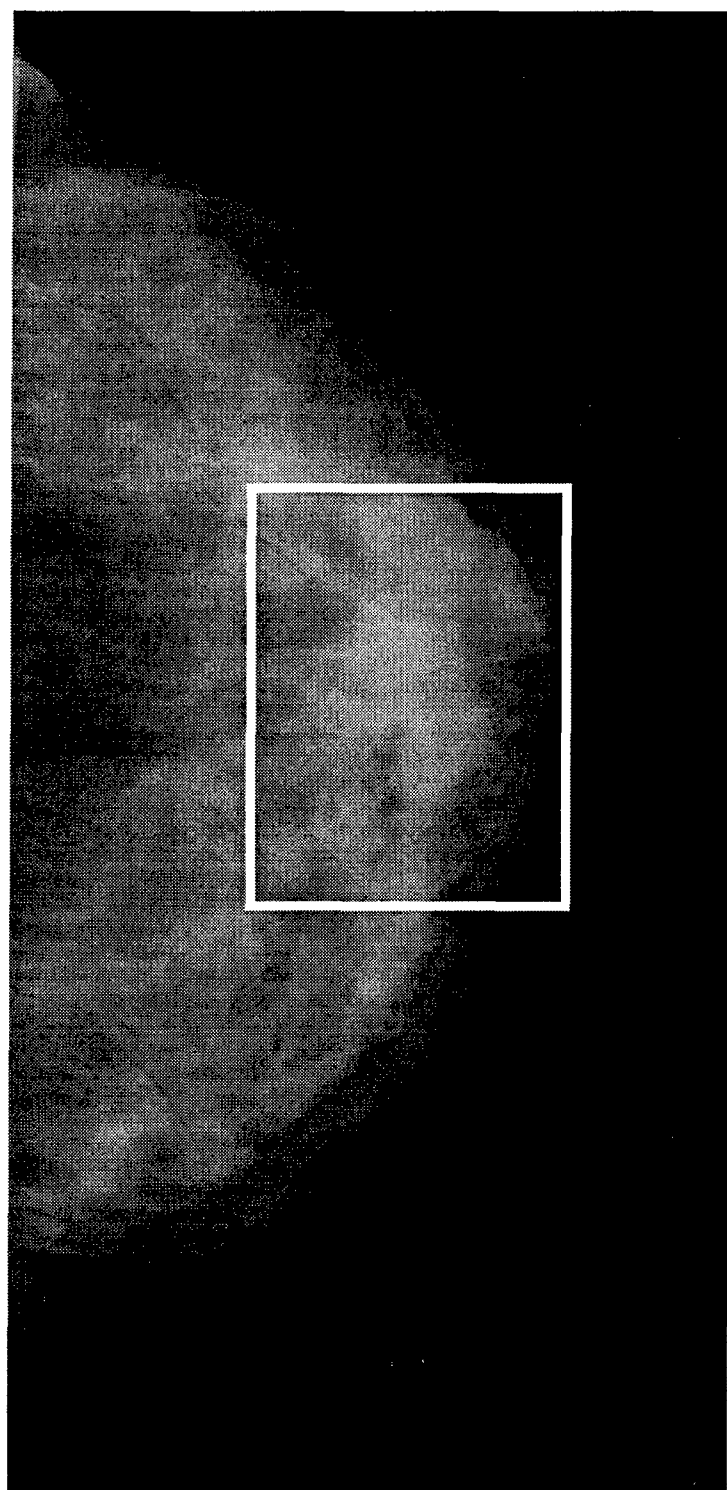
Figure 11 shows the enhancement function from Equation (39) for parameter values $K = 20$ and $T = 1$.

The multiplicative factor obtained as the ratio between the output and input of the enhancement function is next applied to the original wavelet coefficients [26], and then the reconstruction (Figure 3(b) and (d)) is carried out.

Figure 12 shows the cranio-caudal view of a patient with bloody nipple discharge. On the enhanced image cropped to the area of interest, irregular anterior borders of a mass are better seen.

Stellate Lesions

It is important for radiologists to identify stellate lesions since their presence is a serious indicator of malignancy. Stellate lesions vary in size and subtlety and, in addition, do not



(a)



(b)



(c)

Figure 12: Contrast enhancement of the cranio-caudal of a patient with bloody nipple discharge. (a) The original mammogram with area of interest delineated. (b) Unprocessed extracted area. (c) The enhanced area improves the visualization of the mass.

have a clear boundary, making them difficult to detect.

In the development of our algorithm, we follow an observation made by Kegelmeyer *et al.* about the distortion of edge orientation distribution induced by a stellate lesion [35].

Normal mammograms show a roughly radial pattern with structure radiating from the nipple to the chest wall. A stellate lesion not only changes this pattern, but also creates another center from which rays radiate. Directional analysis using the Sobel edge operator was employed for assessment of local orientations [35].

Wavelet transform from Section 2.1 enables directional analysis as well. By adding additional filter $G_{-s}^1(2^m\omega)$ to each scale of decomposition from Figure 3, approximations to both first and second steerable derivatives of a Gaussian are available. A multiscale derivative-pair quadratic feature detector is computed by finding the maximum of the local oriented energy with respect to angle θ

$$E_{2m}^\theta(x, y) = \sqrt{(W1_{2m}^\theta s(x, y))^2 + (W2_{2m}^\theta s(x, y))^2}, \quad (40)$$

where $W1_{2m}^\theta s(x, y)$ and $W2_{2m}^\theta s(x, y)$ denote wavelet decompositions using first (Equation (6) with $d=1$) and second (Equation (6) with $d=2$) derivative wavelet, respectively, steered to angle θ . The angle that maximizes the local oriented energy (40) represents orientation at pixel location (x, y) .

Similarly to the method for enhancement of microcalcifications, processing is carried out within windows with scale dependent sizes: 1-norm of differences between the local and average orientations is computed in the window and used as a measure of orientation nonuniformity. Soft thresholding as a function of the orientation nonuniformity measure is next applied to the transform coefficients at each dyadic scale independently [11]. The altered coefficients are then included for reconstruction.

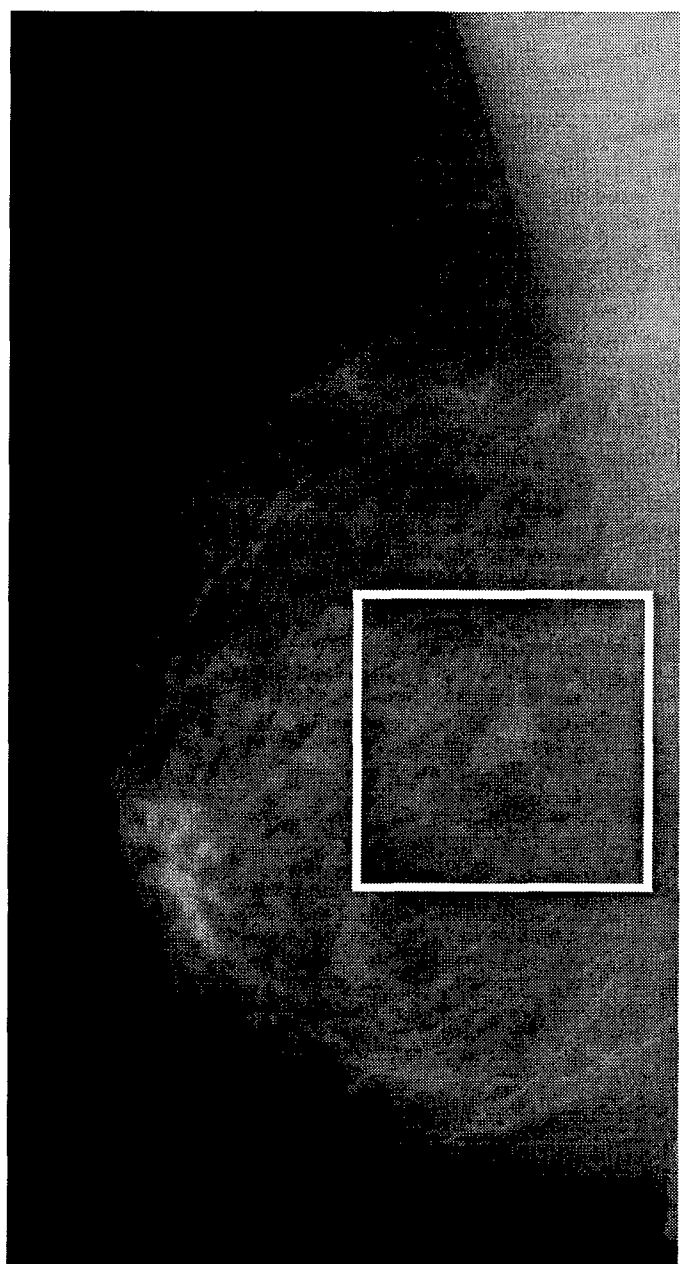
Figure 13 shows the oblique view with a mass visible in the mid-posterior breast. The enhanced image demonstrates the irregularity and spiculation of the mass.

Image fusion of the outputs from the three modules is implicit rather than explicit: wavelet transform coefficients are first modified for enhancement of microcalcifications, circumscribed masses, and stellate lesions, and then the new coefficients are obtained by fusion before the reconstruction is accomplished.

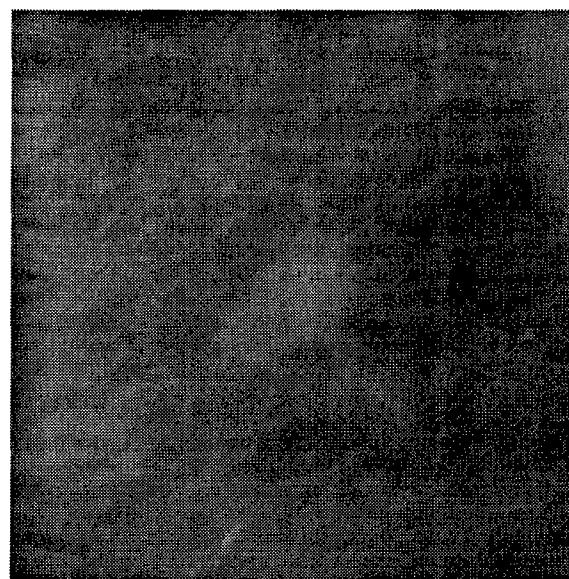
Note also that it is possible to put different weights on features, and exclude certain features from the final result.

2.3 Evaluation

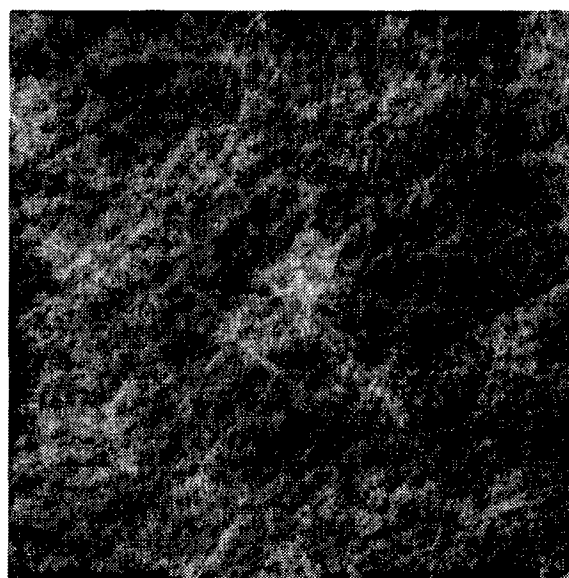
In order to evaluate the contrast enhancement ability of the developed scheme, we compare the performance of the wavelet-based algorithm described in previous sections to results of



(a)



(b)



(c)

Figure 13: Contrast enhancement of the oblique view. (a) The original mammogram with area of interest delineated. (b) Unprocessed extracted area. (c) The enhanced area improves the visibility of the mass.

histogram equalization and unsharp masking.

Histogram is defined as a plot of gray level probabilities versus gray level values in an image. The technique of obtaining a uniform histogram (*i.e.*, uniform gray level distribution) by reassigning gray level values is known as histogram equalization [36]. It is attractive due to its speed and simplicity; however, quantization errors can result in artifacts such as loss of edges [26].

Unsharp masking is based upon smoothing an image with a lowpass filter and then subtracting a fraction of the filtered result from the original image [37]. To better preserve edges in the enhanced image, the median filter is a popular choice for the smoothing filter.

2.3.1 Image Phantoms

We conducted a set of experiments using computer simulated phantoms similar to the ones generated by Xing *et al.* [38].

The phantoms consisted of a 505×505 image matrix with 8 bits per pixel (*i.e.*, 256 levels of gray) divided into 25 (5×5 grid) 101×101 pixel squares. Twelve randomly distributed squares contained a truncated Gaussian shaped signal with the peak signal intensity I ($15 \leq I \leq 35$) levels above the background level and the radius of the signal set to 25 pixels. Random Gaussian noise with the mean value of 128 and the standard deviation σ ($20 \leq \sigma \leq 80$) was added to the image matrix. Figure 14(a) demonstrates a distribution of signal squares within the phantom, and Figure 14(b) shows the phantom with noise.

By choosing different values of the peak signal intensity and of the noise variance we can alter the visibility of the Gaussian signals. In the course of experiments with different peak signal intensities and noise variances, we compared the ability of the three contrast enhancement methods to improve the visibility of signals embedded in noise. We adopted quantitative criteria for measuring the performance of contrast enhancement algorithms employed by Xing *et al.* [38]—the enhancement factor EF was given as the ratio between the output and input contrast-to-noise ratio

$$EF = \frac{CNR_o}{CNR_i},$$

where the contrast-to-noise ratio CNR was defined as the ratio between contrast

$$C = \frac{1}{M_s} \sum_{m=1}^{M_s} \frac{(S_m - B_m)}{P_m}$$

and noise

$$N = \frac{1}{M_s} \sum_{m=1}^{M_s} \sigma_{B_m}$$

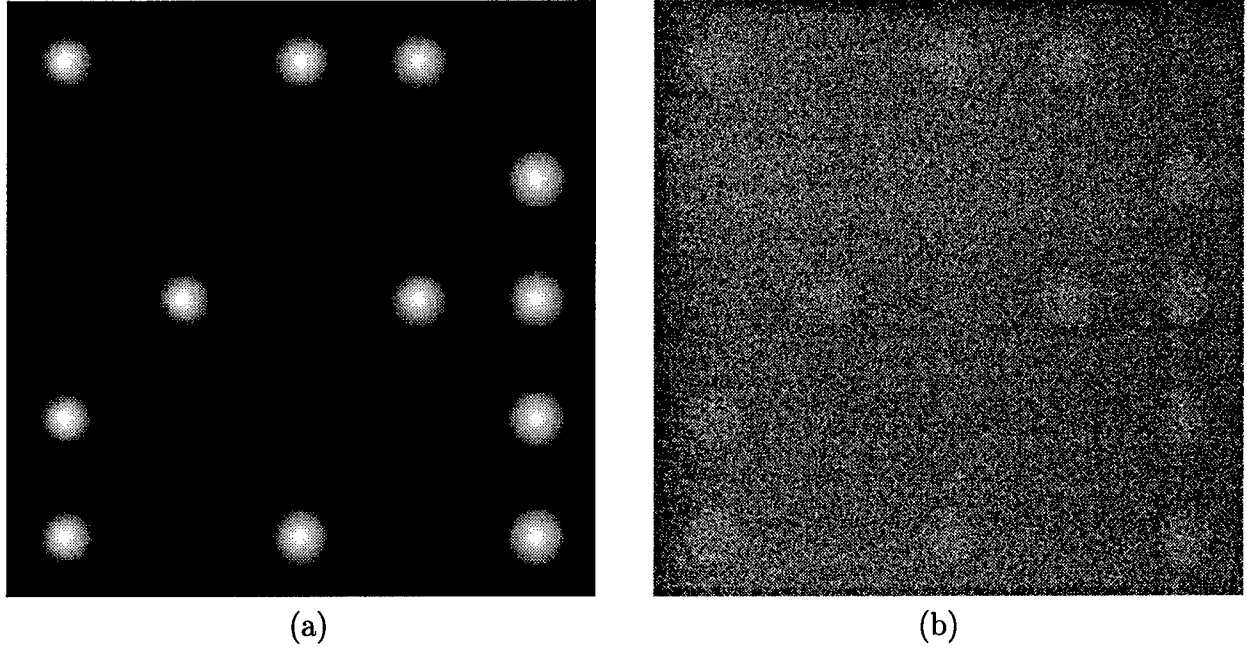


Figure 14: Generation of image phantoms. (a) A distribution of truncated Gaussian signals. (b) A phantom obtained by adding noise to the image from (a).

with S_m and B_m denoting the gross count over circular signal area in signal and background squares, respectively, P_m standing for the number of pixels in the m -th signal area, M_s being equal to the number of squares containing the signal, and σ_{B_m} meaning the standard deviation in the circular area over which B_m was computed.

Phantom images were generated using the sets of values $I = \{15, 25, 35\}$ and $\sigma = \{20, 30, 40, 50, 60, 70, 80\}$, and contrast C and noise N were computed for both the phantom images and enhanced images obtained via the three methods. These numerical results are summarized in Table 7.

The behavior of the three methods in this experimental setup was quite different. Histogram equalization proved to be the most sensitive to the level of noise. In general it resulted in the largest contrast improvement among the three; however, it also increased the level of noise the most. The resulting contrast was inversely proportional to the level of noise, and, interestingly, the noise after enhancement was pretty much independent of noise in the input image. It is worth mentioning that in low to moderate noise conditions the numbers in Table 7 do not convey observers' perceptual experience faithfully; histogram equalization made objects more visible while noise, although increased, was still acceptable to viewers.

Unsharp masking, on the other hand, was not able to increase contrast, but it dealt well with noise. Except for the lowest noise cases, it always resulted in less noise in the enhanced

Table 7: Contrast enhancement of image phantoms by means of histogram equalization (HE), unsharp masking (UM), and wavelet transform (WT).

I	σ	C	N	C_{HE}	N_{HE}	EF_{HE}	C_{UM}	N_{UM}	EF_{UM}	C_{WT}	N_{WT}	EF_{WT}
15	20	10.0525	19.8332	35.4784	73.5423	0.9518	9.4999	24.3040	0.7712	21.2574	25.0783	1.6724
15	30	10.0259	29.7497	23.9383	74.1127	0.9584	7.2788	27.9429	0.7729	17.4259	22.1221	2.3374
15	40	9.9801	39.6290	17.9857	74.2963	0.9613	6.6398	34.1014	0.7731	13.3124	19.4391	2.0321
15	50	9.8363	49.0628	14.3026	74.2479	0.9609	6.5020	42.1009	0.7703	10.2670	18.2236	2.8102
15	60	9.5601	57.6065	11.8676	74.2017	0.9637	6.2683	49.2904	0.7663	9.7388	19.5359	3.0039
15	70	9.1465	65.1124	10.1187	74.2453	0.9702	5.9212	55.6558	0.7574	9.7907	20.9298	3.3301
15	80	8.6422	71.5364	8.8012	74.2608	0.9810	5.4977	61.0133	0.7459	10.7956	23.2167	3.8490
25	20	16.7882	19.8332	56.9599	73.2214	0.9190	15.8346	24.3040	0.7697	23.7076	27.4536	1.0202
25	30	16.7609	29.7497	39.3872	73.8557	0.9466	12.1397	27.9428	0.7711	22.2295	26.1766	1.5073
25	40	16.6970	39.6290	29.8402	73.9618	0.9576	11.0159	33.8819	0.7717	19.8742	24.1919	1.9498
25	50	16.4722	49.0628	23.9912	74.2363	0.9626	10.7931	41.7790	0.7695	17.4175	22.7817	2.2772
25	60	16.0189	57.6065	19.9839	74.1521	0.9692	10.3981	48.9549	0.7638	16.2716	23.3417	2.5069
25	70	15.3817	65.1124	17.0857	74.0931	0.9761	9.8328	55.1926	0.7542	15.7445	26.0267	2.5608
25	80	14.5902	71.5364	14.9119	74.1410	0.9862	9.1674	60.5561	0.7423	15.5779	26.4523	2.8874
35	20	23.5240	19.8332	74.8037	72.2778	0.8726	22.1709	24.3040	0.7691	23.7807	24.5468	0.8168
35	30	23.4946	29.7497	53.5694	73.3056	0.9253	16.9934	27.9419	0.7701	23.8696	26.6390	1.1346
35	40	23.4005	39.6290	41.2118	73.7483	0.9464	15.2950	33.6426	0.7699	23.9136	28.6561	1.4132
35	50	23.0711	49.0628	33.3156	73.9330	0.9583	14.9661	41.4438	0.7680	23.1115	28.6185	1.7174
35	60	22.4270	57.6065	27.8817	73.9846	0.9680	14.4224	48.6344	0.7617	22.7287	30.6786	1.9030
35	70	21.5545	65.1124	23.9775	74.0517	0.9781	13.6476	54.7661	0.7528	21.8585	30.3670	2.1744
35	80	20.4740	71.5364	20.9949	74.1379	0.9895	12.7414	60.0949	0.7408	20.6772	30.3359	2.3815

image. The combination of loss of contrast and marginal noise improvement, however, resulted in worse visibility than in the original images. This is no surprise considering the nature of the experiment: the Gaussian shaped objects are comprised primarily of lower frequencies while unsharp masking was designed to emphasize higher frequencies.

The wavelet transform based approach was the only one that resulted in enhancement factors greater than one. It was consistently improving contrast and generally lowering the amount of noise. High noise cases were the ones where this method really shined while at low levels of noise, the noise was, as in unsharp masking, amplified in the enhanced image. The method did no good when the signal was strong and noise marginal ($I = 35$, $\sigma = 20$), and such conditions also produced the worse enhancement factor in histogram equalization. Figure 15 displays an example of moderately visible objects. It can be observed that histogram equalization improved visibility despite its enhancement factor being below one, unsharp masking resulted in less noise but less contrast as well, and wavelet transform yielded the best results. The same signal constellation was used in Figure 16. Here, one can hardly notice any signal activity in the original or the histogram equalized image, while the wavelet transform based method brings out the signal areas nicely.

Please note that the probability density functions for signals and noise in these image phantom are not only known but also very simple. None of the tested methods is taking advantage of this fact; however, it would be easy to devise one and achieve the best results for this particular set of experiments. Such limiting the scope of a method, of course, would be diverting from the original goal—enhancement of mammographic features.

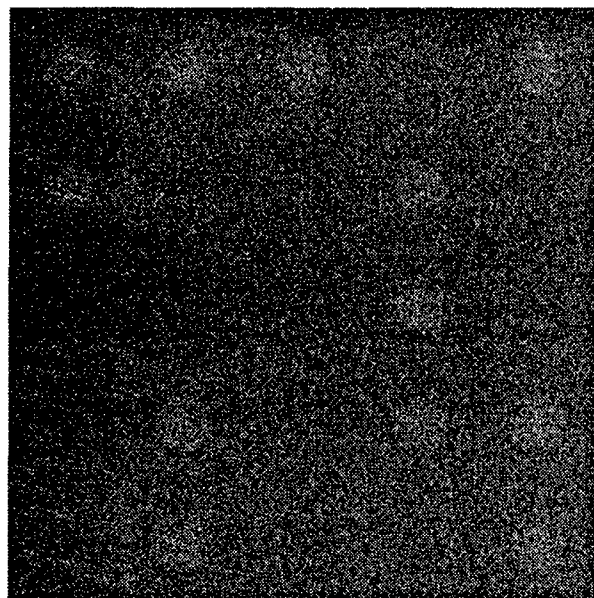
2.3.2 Phantoms Blended Into Mammograms

To compare the performance of histogram equalization, unsharp masking, and wavelet based enhancement on mammographic images, we constructed three mathematical models of phantoms similar in appearance to the ones used by Chang and Laine [39] and Laine *et al.* [25]. The models including features found in circumscribed masses, spiculate lesions, and microcalcifications are shown in Figure 17.

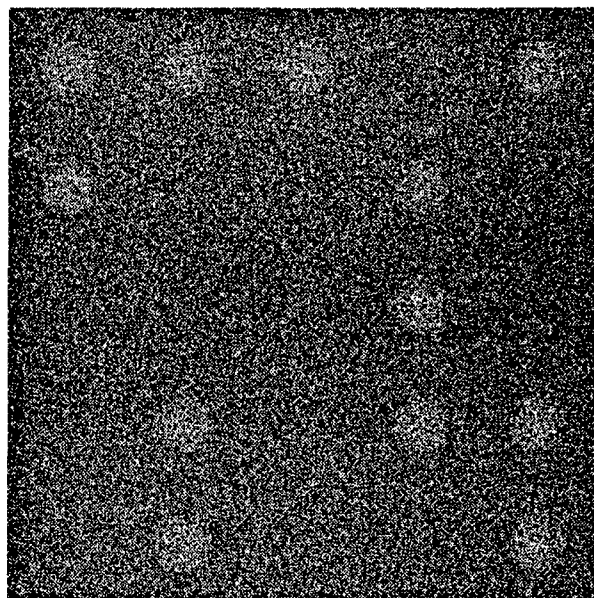
These models of varying intensity, size, and rotation were blended into mammograms to be processed by the three enhancement techniques under comparison. Quantitative metric for assessing the performance of the techniques was adopted after Laine *et al.* [25]: a contrast improvement index

$$CII = \frac{C_{\text{Processed}}}{C_{\text{Original}}}$$

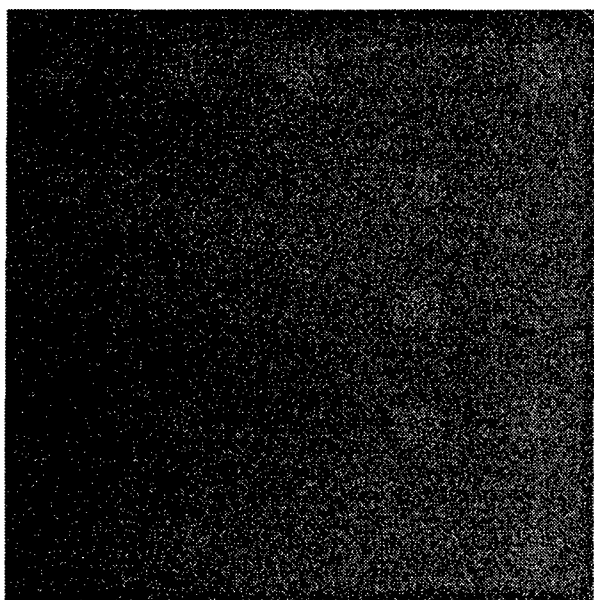
was computed between the processed and original contrast in the rectangular region of interest snugly fitting a phantom.



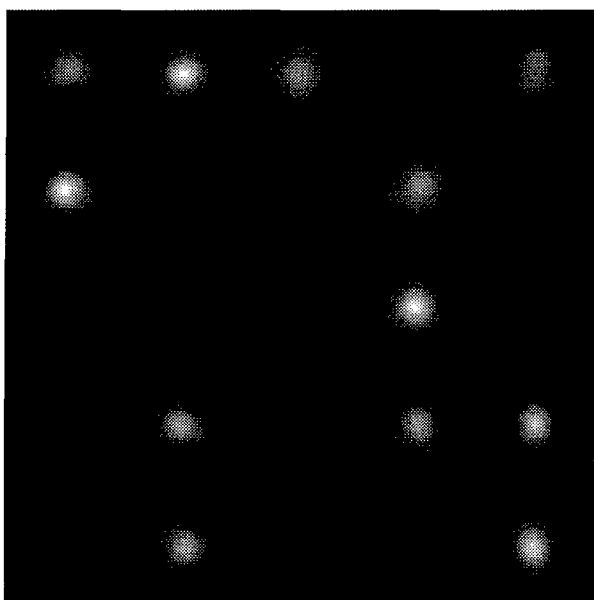
(a)



(b)

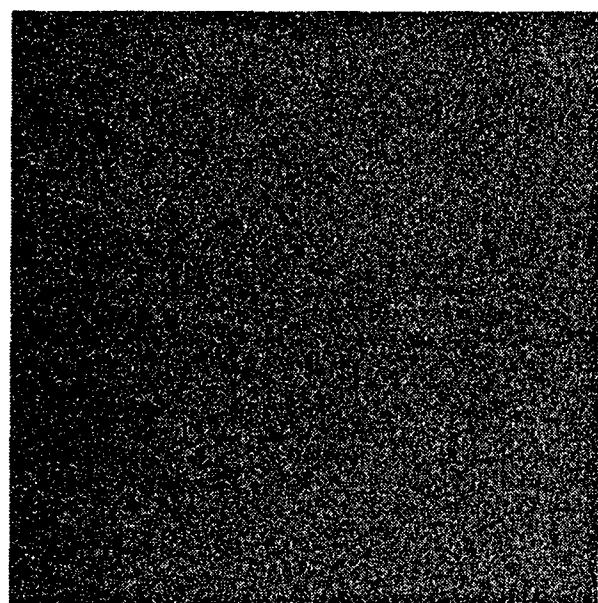


(c)

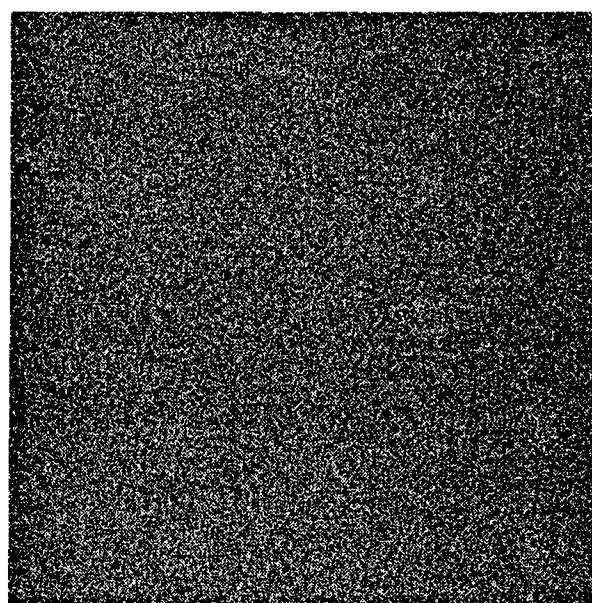


(d)

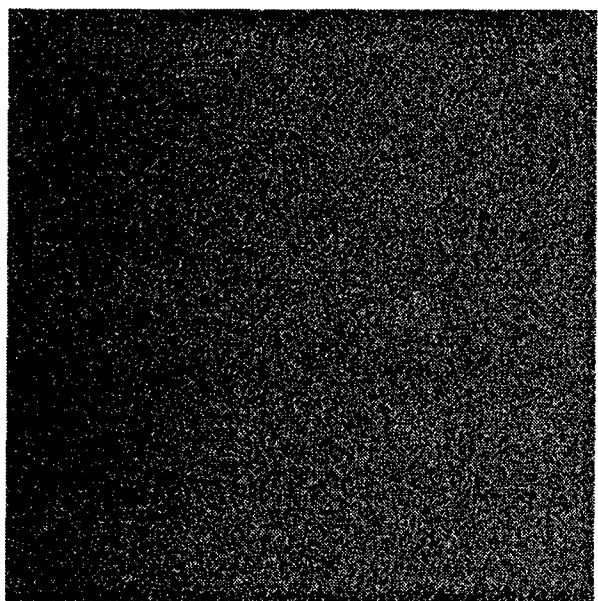
Figure 15: Image phantom contrast enhancement. (a) Image phantom ($I = 35$, $\sigma = 40$). (b) Histogram equalization. (c) Unsharp masking. (d) Wavelet transform based enhancement.



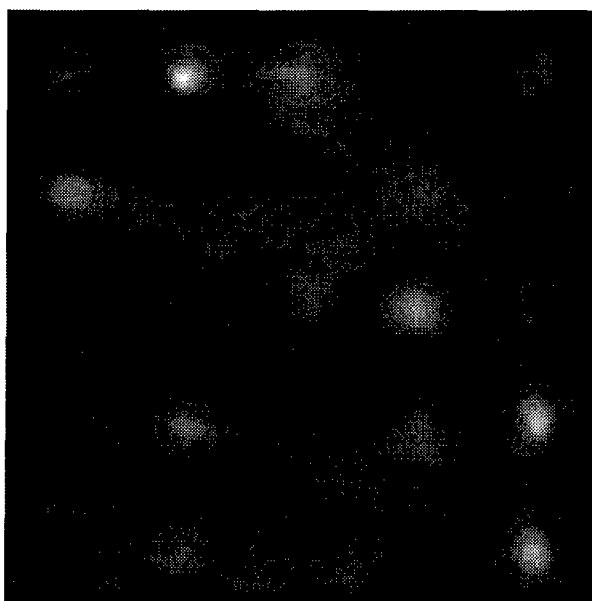
(a)



(b)



(c)



(d)

Figure 16: Image phantom contrast enhancement. (a) Image phantom with the same signal constellation as in Figure 15 ($I = 15$, $\sigma = 60$). (b) Histogram equalization. (c) Unsharp masking. (d) Wavelet transform based enhancement.

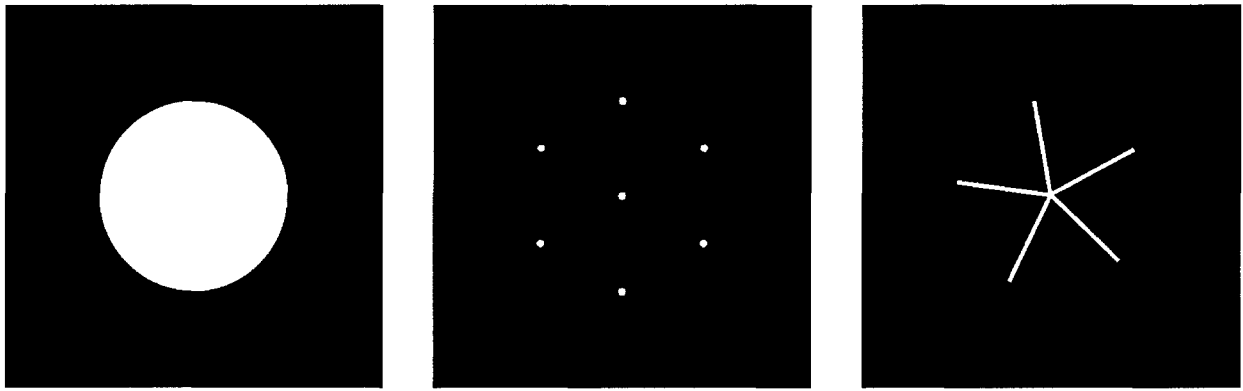


Figure 17: Mathematical phantoms that were blended into mammographic images.

The contrast was defined as

$$C = \frac{f - b}{f + b}$$

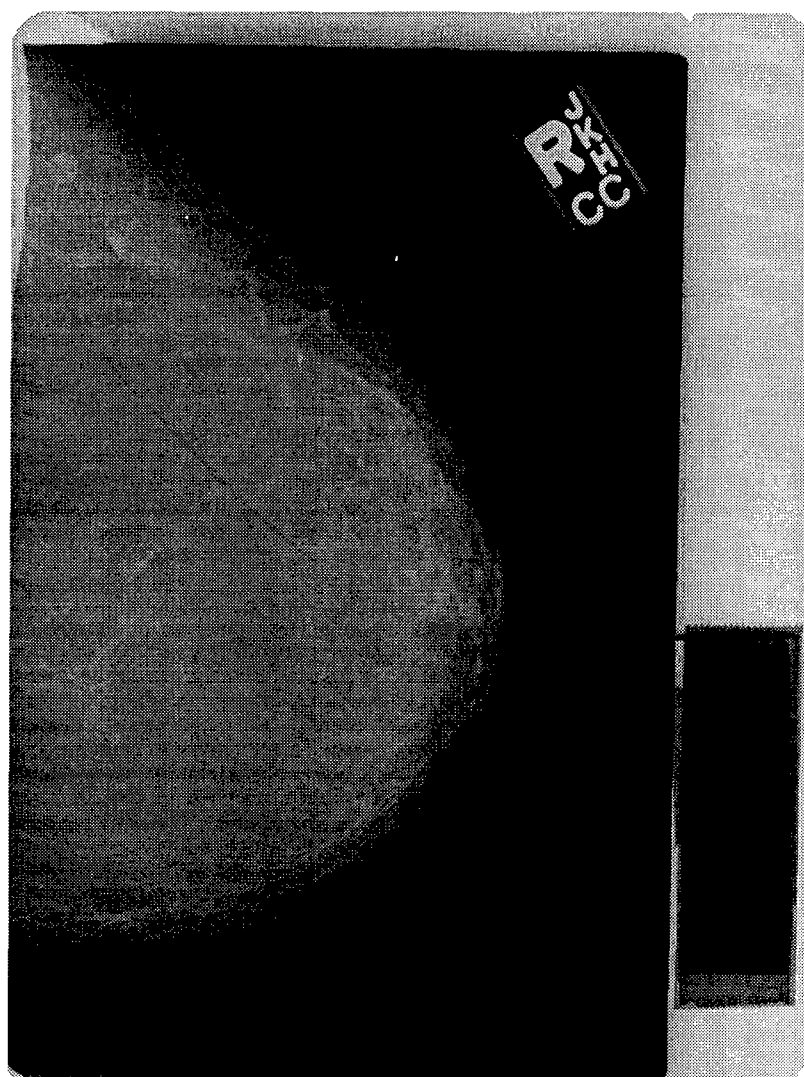
with f and b denoting foreground (*i.e.*, phantom pixels) and background (*i.e.*, pixels in the rectangular area surrounding the phantom), respectively.

Note that the input (reference) mammograms for this set of experiments were obtained by applying contrast stretching to digitized mammograms. The reason for this is that we wanted to avoid a commonly used “trick” in presenting the results of enhancement: original mammograms that occupy only a portion of the available dynamic range are left as they are while the enhancement algorithm output utilizes the entire dynamic range. We level the playing field by forcing the same dynamic range upon both original and enhanced images. The right cranio-caudal view of Figure 18 shows a circumscribed mass phantom blended near the upper left corner of the image of matrix size 1553×2048 while the original and enhanced region of interest of size 121×121 are displayed underneath it.

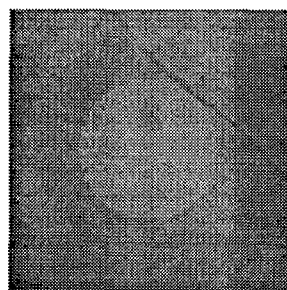
On the oblique medio-lateral view presented on Figure 19 of the same size, blended microcalcifications phantom slightly up and left from the center of the film is practically invisible. The 81×81 region of interest is used to compare the outputs of the three contrast enhancement methods.

Finally, Figure 20 presents an example of a spiculate lesion phantom enhancement. The phantom is too thin to be visible in the upper right corner of the mammographic image of size 1553×2048 , but it does appear on the extracted 81×81 region of interest from the original and the enhanced images.

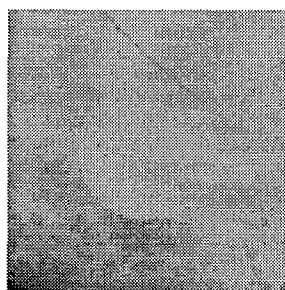
Comparison of the enhancement methods by means of both visual appearance and quantitative criteria demonstrated that the wavelet based approach outperformed histogram equalization and unsharp masking. The CII values given in Tables 8, 9, and 10 for different mammograms, phantom intensities, sizes, and orientations show that



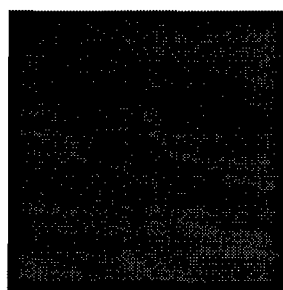
(a)



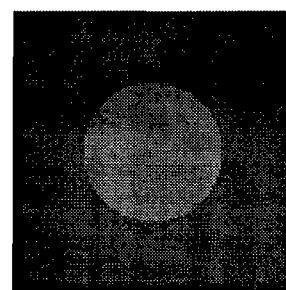
(b)



(c)

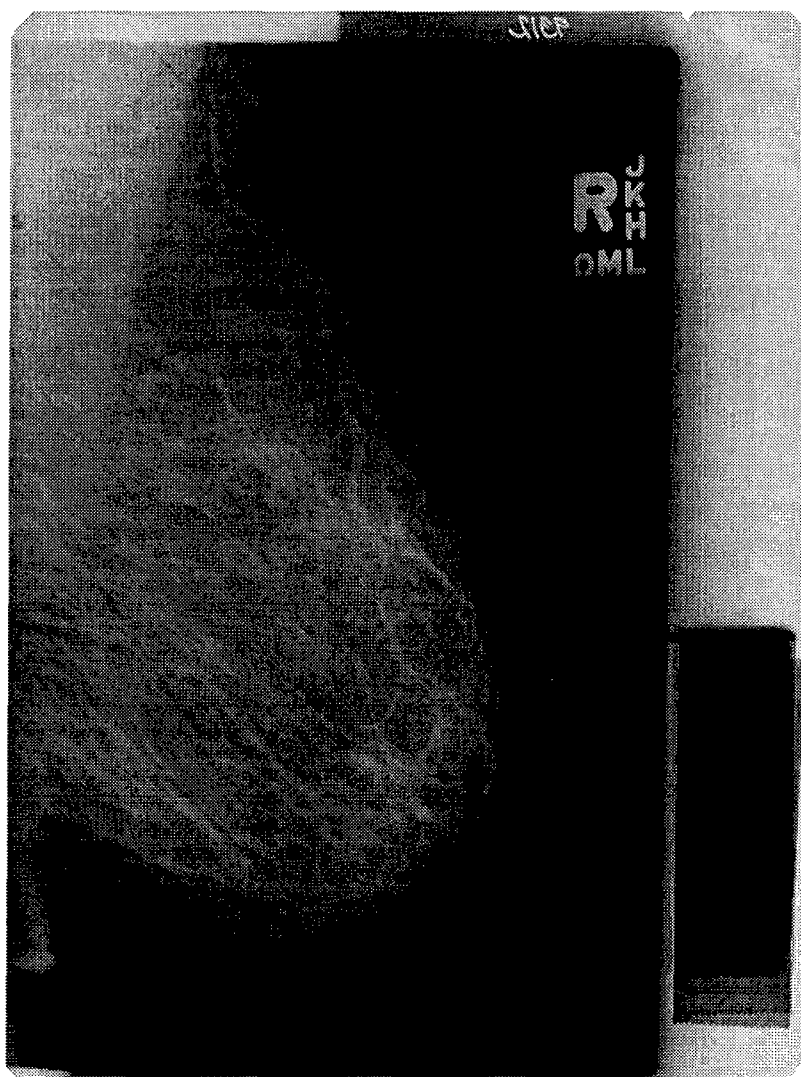


(d)

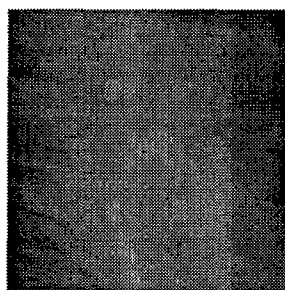


(e)

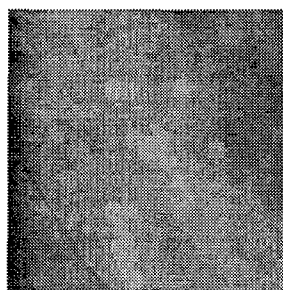
Figure 18: Contrast enhancement of a mass resembling phantom. (a) Original mammogram with a phantom blended near the upper left corner. (b) Region of interest from the original mammogram. (c) Histogram equalization. (d) Unsharp masking. (e) Wavelet transform based enhancement.



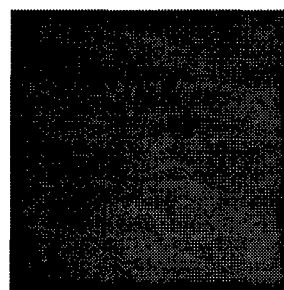
(a)



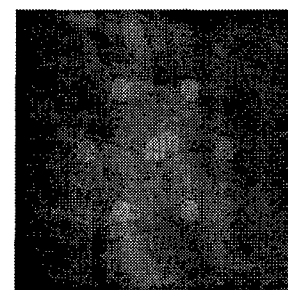
(b)



(c)

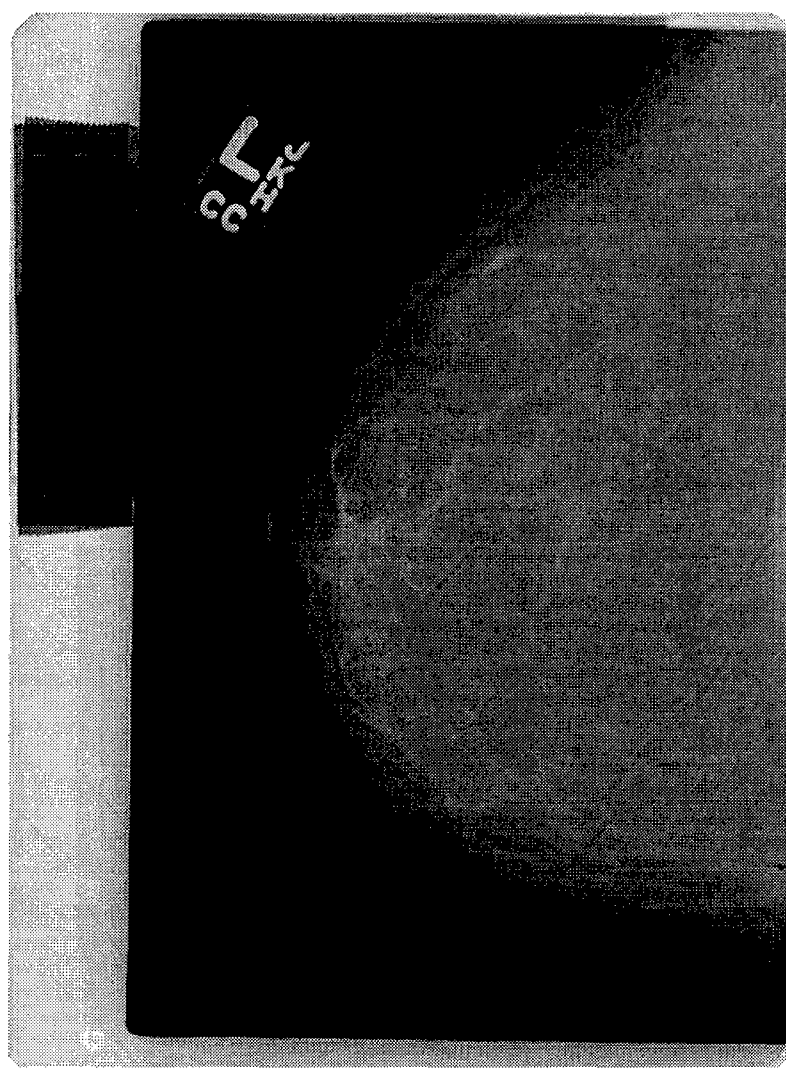


(d)

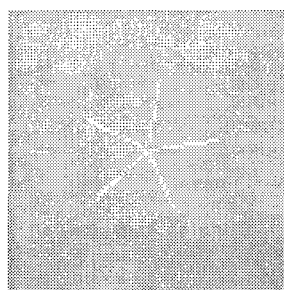


(e)

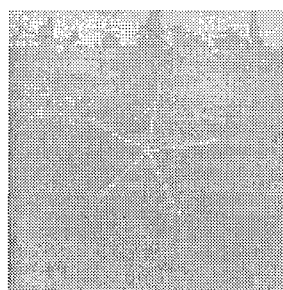
Figure 19: Contrast enhancement of a microcalcifications resembling phantom. (a) Original mammogram with a phantom blended slightly up and left from the center of the film. (b) Region of interest from the original mammogram. (c) Histogram equalization. (d) Unsharp masking. (e) Wavelet transform based enhancement.



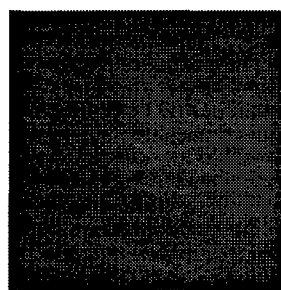
(a)



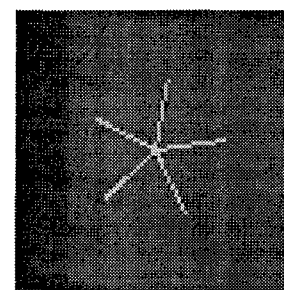
(b)



(c)



(d)



(e)

Figure 20: Contrast enhancement of a microcalcifications resembling phantom. (a) Original mammogram with a phantom blended slightly up and left from the center of the film. (b) Region of interest from the original mammogram. (c) Histogram equalization. (d) Unsharp masking. (e) Wavelet transform based enhancement.

Table 8: Contrast enhancement of circumscribed mass phantoms by means of histogram equalization (HE), unsharp masking (UM), and wavelet transform (WT).

Case	CII _{HE}	CII _{UM}	CII _{WT}
1	1.6917	1.4749	2.4790
2	0.6368	0.5615	2.5695
3	1.1028	0.5702	2.9598
4	0.7780	0.5644	3.5478
5	2.1308	0.4583	1.5779
6	0.6249	0.6345	3.0910
7	1.9501	1.2311	2.6068
8	1.4860	0.8913	2.7621
9	1.4565	1.0185	1.8214
10	0.9218	0.7382	2.1763

Table 9: Contrast enhancement of circumscribed mass phantoms by means of histogram equalization (HE), unsharp masking (UM), and wavelet transform (WT).

Case	CII _{HE}	CII _{UM}	CII _{WT}
1	0.5335	1.3471	3.0844
2	1.1018	0.9552	2.4362
3	1.8519	0.8615	2.3966
4	0.9553	0.9345	2.3869
5	1.4057	0.9355	2.9169
6	1.4103	0.8936	3.0579
7	1.3529	0.8132	3.0099
8	1.1389	1.2028	3.1987
9	0.6038	1.2722	2.7468
10	1.4451	1.4660	3.4186

histogram equalization outperformed wavelet transform based enhancement in certain situations. This is due to the fact that the phantom has basically no effect on the gray level distribution, and its gray levels sometimes simply got quantized to high enough a value for a significant contrast improvement. More than inconsistency of histogram equalization is worrisome its tendency to introduce artifacts. This was particularly obvious in enhancement of microcalcifications phantoms; as exhibited in Figure 19(c), the circles were completely distorted. Unsharp masking was both consistent and artifact free, but unfortunately resulted in least enhancement. It seems that the images were too complex and the phantoms too subtle for unsharp masking to make a difference.

Table 10: Contrast enhancement of spiculate lesion phantoms by means of histogram equalization (HE), unsharp masking (UM), and wavelet transform (WT).

Case	CII_{HE}	CII_{UM}	CII_{WT}
1	2.3008	1.3125	3.3071
2	1.8462	1.2026	2.6721
3	0.8381	1.0196	1.8813
4	1.3795	0.8318	2.5028
5	1.7095	1.4289	2.3046
6	2.1897	1.1934	1.9822
7	1.3028	0.5417	2.1509
8	2.6979	1.3784	2.8600
9	2.8537	0.5936	2.4966
10	0.8998	0.8216	2.6449

3 Key Research Accomplishments

- A redundant wavelet transform that enables artifact-free translation and rotation invariant processing was constructed and efficiently implemented as a bank of digital filters.
- A modular scheme for fusion of locally enhanced mammographic features was devised such that enhancement algorithms targeting specific features can be further developed and optimized separately from the fusion mechanism.
- The derived wavelet transform proved to be more suitable for image fusion than traditional orthogonal/biorthogonal wavelet transforms and image pyramids.
- Quantitative evaluation gave the wavelet based enhancement technique an edge over histogram equalization and unsharp masking while at the same time no harmful artifacts emanating from the wavelet method were observed.

4 Reportable Outcomes

Publications

- [1] I. Koren, A. Laine, S. Smith, E. Nickoloff, and F. Taylor, "Visualization of mammograms via fusion of enhanced features," in K. Doi, H. MacMahon, M. L. Giger, and K. R. Hoffmann, Eds., *Computer-Aided Diagnosis in Medical Imaging*, Amsterdam, The Netherlands: Elsevier, 1999.
- [2] I. Koren, A. Laine, and F. Taylor, "Enhancement via fusion of mammographic features," in *Proc. IEEE Int. Conf. Image Process.*, Chicago, IL, Oct. 1998, vol. 1, pp. 722–726.
- [3] I. Koren and A. Laine, "A discrete dyadic wavelet transform for multidimensional feature analysis," in M. Akay (Editor), *Time-Frequency and Wavelets in Biomedical Signal Engineering*, New York, NY: IEEE Press, 1998, pp. 425–449.
- [4] I. Koren, A. Laine, and F. Taylor, "An overcomplete enhancement of digital mammograms," *Era of Hope, A Multidisciplinary Reporting of DoD Progress*, Washington, D.C., Oct.–Nov. 1997, vol. 1, pp. 107–108.
- [5] A. F. Laine, I. Koren, S. Schuler, W. Huda, and B. G. Steinbach, "Contrast enhancement of mammographic features via multiscale analysis," *RSNA 82nd Scientific Assembly and Annual Meeting*, Chicago, IL, 1996.

Funded Research

National Cancer Institute, National Institutes of Health, "Athena Mammographic Technology," 1999 to 2000, \$125,000; Iztok Koren, Principal Investigator.

Employment

The Athena Group, Inc., Gainesville, FL. Iztok Koren, development of mammographic image manipulation and enhancement system.

5 Conclusions

In the course of this project, we developed a method that improves the visibility of specific mammographic features by local enhancement and fusion of the enhanced areas. The described method incorporates a variety of properties of mammographic image enhancement methods tailored to specific signs of malignancy into a unified computational framework.

Our method is based upon a wavelet transform which we constructed such that its analysis stage enabled approximations to directional first and second derivatives of a Gaussian function and to Laplacian of Gaussian across distinct scales. Such a decomposition is suitable for both anisotropic and isotropic multiscale analysis, and, in addition, provides an adaptable framework for incorporation of a variety of mammographic processing methods. The derived steerable dyadic wavelet transform has also proved flexible enough for enhancement and fusion of individual types of mammographic features. Separate enhancement algorithms have been developed for microcalcifications, circumscribed masses, and stellate lesions, and fusion of the modified transform coefficients performed before the reconstruction of the final enhanced image. The devised algorithm is also well suited for further refinements; optimizations can be performed for each type of malignancy alone, and separately for the fusion module.

It is of prime importance that neither the enhancement nor the fusion process introduce any artifacts that could adversely impact the radiologists' decisions. We compared the steerable dyadic wavelet transform with the gradient pyramid, orthogonal wavelet transform, and biorthogonal wavelet transform for fusion of features relevant to mammography. During our experiments, the steerable dyadic wavelet transform was exhibiting a combination of best properties of the gradient pyramid and of the orthogonal/biorthogonal wavelet transform. The steerable dyadic wavelet transform behaved similarly as the gradient pyramid in a sense that it did not introduce artifacts commonly present when the orthogonal and biorthogonal wavelet transforms were used. At the same time, the steerable dyadic wavelet transform outperformed the gradient pyramid by acting like the orthogonal and biorthogonal wavelet transforms in terms of mathematical criteria and sharpness in the fused image.

Our final task was evaluation of the developed wavelet based enhancement method. We adopted quantitative criteria to measure the performance of our contrast enhancement technique on simulated phantoms embedded in noise and on mammographic feature phantoms blended into mammograms. The wavelet based method outperformed histogram equalization and unsharp masking with respect to both quantitative criteria and absence of

undesirable artifacts.

This work represents an important step towards development of a system which can be deployed in a clinical setting. In order to get closer to that goal, a receiver operating characteristic (ROC) study which was unfortunately beyond the scope of this project will have to be carried out.

References

- [1] S. H. Landis, T. Murray, S. Bolden, and P. A. Wingo, "Cancer statistics, 1999," *CA Cancer J. Clin.*, vol. 49, no. 1, pp. 8–31, 1999.
- [2] R. A. Smith, "Epidemiology of breast cancer," in *A Categorical Course in Physics, Technical Aspects of Breast Imaging*, A. G. Haus and M. J. Yaffe, Eds. The 79th Scientific Assembly and Annual Meeting of the Radiological Society of North America (RSNA), 1993, pp. 21–33.
- [3] M. J. T. Smith and T. P. Barnwell, III, "Exact reconstruction techniques for tree-structured subband coders," *IEEE Trans. Acoust. Speech Signal Process.*, vol. 34, no. 3, pp. 434–441, 1986.
- [4] P. J. Burt and E. H. Adelson, "The Laplacian pyramid as a compact image code," *IEEE Trans. Commun.*, vol. 31, no. 4, pp. 532–540, 1983.
- [5] A. Witkin, "Scale space filtering," in *Proc. Int. Joint Conf. Artif. Intell.*, Karlsruhe, Germany, 1983, pp. 1019–1022.
- [6] I. Daubechies, *Ten Lectures on Wavelets*, SIAM, Philadelphia, PA, 1992.
- [7] M. Holschneider, R. Kronland-Martinet, J. Morlet, and Ph. Tchamitchian, "A real-time algorithm for signal analysis with the help of the wavelet transform," in *Wavelets, Time-Frequency Methods and Phase Space*, J. M. Combes, A. Grossmann, and Ph. Tchamitchian, Eds., Springer-Verlag, Berlin, Germany, 1989, pp. 286–297.
- [8] J. Canny, "A computational approach to edge detection," *IEEE Trans. Pattern Anal. Mach. Intell.*, vol. 8, no. 6, pp. 679–698, 1986.
- [9] W. T. Freeman and E. H. Adelson, "The design and use of steerable filters," *IEEE Trans. Pattern Anal. Mach. Intell.*, vol. 13, no. 9, pp. 891–906, 1991.
- [10] J. Babaud, A. P. Witkin, M. Baudin, and R. O. Duda, "Uniqueness of the Gaussian kernel for scale-space filtering," *IEEE Trans. Pattern Anal. Mach. Intell.*, vol. 8, no. 1, pp. 26–33, 1986.
- [11] I. Koren, A. Laine, F. Taylor, and M. Lewis, "Interactive wavelet processing and techniques applied to digital mammography," in *Proc. IEEE Int. Conf. Acoust. Speech Signal Process.*, Atlanta, GA, 1996, vol. 3, pp. 1415–1418.

- [12] I. Koren, *A multiscale spline derivative-based transform for image fusion and enhancement*, PhD thesis, Department of Electrical and Computer Engineering, University of Florida, Gainesville, FL, 1996.
- [13] A. J. Jerri, "The Shannon sampling theorem—its various extensions and applications: A tutorial review," *Proc. IEEE*, vol. 65, no. 11, pp. 1565–1596, 1977.
- [14] I. Koren and A. Laine, "A discrete dyadic wavelet transform for multidimensional feature analysis," in *Time-Frequency and Wavelets in Biomedical Signal Engineering*, M. Akay, Ed., IEEE Press, New York, NY, 1997, pp. 425–449.
- [15] A. V. Oppenheim and R. W. Schaffer, *Discrete-Time Signal Processing*, Prentice-Hall, Englewood Cliffs, NJ, 1989.
- [16] O. Rioul and P. Duhamel, "Fast algorithms for discrete and continuous wavelet transforms," *IEEE Trans. Inf. Theory*, vol. 38, no. 2, pp. 569–586, 1992.
- [17] M. Unser, A. Aldroubi, and M. Eden, "Fast B-spline transforms for continuous image representation and interpolation," *IEEE Trans. Pattern Anal. Mach. Intell.*, vol. 13, no. 3, pp. 277–285, 1991.
- [18] P. J. Burt and R. J. Kolczynski, "Enhanced image capture through fusion," in *Proc. Int. Conf. Comput. Vision*, Berlin, Germany, 1993, pp. 173–182.
- [19] A. Toet, "Image fusion by a ratio of low-pass pyramid," *Pattern Recognit. Lett.*, vol. 9, no. 4, pp. 245–253, 1989.
- [20] L. J. Chipman, T. M. Orr, and L. N. Graham, "Wavelets and image fusion," in *Proc. IEEE Int. Conf. Image Process.*, Washington, D.C., 1995, vol. 3, pp. 248–251.
- [21] I. Koren, A. Laine, and F. Taylor, "Image fusion using steerable dyadic wavelet transform," in *Proc. IEEE Int. Conf. Image Process.*, Washington, D.C., 1995, vol. 3, pp. 232–235.
- [22] H. Li, B. S. Manjunath, and S. K. Mitra, "Multi-sensor image fusion using the wavelet transform," in *Proc. IEEE Int. Conf. Image Process.*, Austin, TX, 1994, vol. 1, pp. 51–55.
- [23] T. Ranchin, L. Wald, and M. Mangolini, "Efficient data fusion using wavelet transform: the case of SPOT satellite images," in *Mathematical Imaging: Wavelet Applications in Signal and Image Processing*, Proc. SPIE, A. F. Laine, Ed., San Diego, CA, 1993, vol. 2034, pp. 171–178.

- [24] S. G. Mallat, "A theory for multiresolution signal decomposition: the wavelet representation," *IEEE Trans. Pattern Anal. Mach. Intell.*, vol. 11, no. 7, pp. 674-693, 1989.
- [25] A. F. Laine, S. Schuler, J. Fan, and W. Huda, "Mammographic feature enhancement by multiscale analysis," *IEEE Trans. Med. Imaging*, vol. 13, no. 4, pp. 725-740, 1994.
- [26] J. Fan and A. Laine, "Multiscale contrast enhancement and denoising in digital radiographs," in *Wavelets in Medicine and Biology*, A. Aldroubi and M. Unser, Eds., CRC Press, Boca Raton, FL, 1996, pp. 163-189.
- [27] C.-M. Chang and A. Laine, "Enhancement of mammograms from oriented information," in *Proc. IEEE Int. Conf. Image Process.*, Santa Barbara, CA, 1997, vol. 3, pp. 524-527.
- [28] W. M. Morrow, R. B. Paranjape, R. M. Rangayyan, and J. E. L. Desautels, "Region-based contrast enhancement of mammograms," *IEEE Trans. Med. Imaging*, vol. 11, no. 3, pp. 392-406, 1992.
- [29] R. N. Strickland and H. I. Hahn, "Wavelet transforms for detecting microcalcifications in mammograms," *IEEE Trans. Med. Imaging*, vol. 15, no. 2, pp. 218-229, 1996.
- [30] H. Yoshida, W. Zhang, W. Cai, K. Doi, R. M. Nishikawa, and M. L. Giger, "Optimizing wavelet transform based on supervised learning for detection of microcalcifications in digital mammograms," in *Proc. IEEE Int. Conf. Image Process.*, 1995, vol. 3.
- [31] L. W. Estevez and N. D. Kehtarnavaz, "Computer assisted enhancement of mammograms for detection of microcalcifications," in *Proc. IEEE Symp. Comput. Based Med. Syst.*, 1995, pp. 16-23.
- [32] H. Li, K. J. R. Liu, and S. C. B. Lo, "Fractal modeling of mammogram and enhancement of microcalcifications," in *Proc. IEEE Nucl. Sci. Symp. Med. Imaging Conf.*, 1997, vol. 3, pp. 1850-1854.
- [33] M. Unser, A. Aldroubi, and M. Eden, "On the asymptotic convergence of B-spline wavelets to Gabor functions," *IEEE Trans. Inf. Theory*, vol. 38, no. 2, pp. 864-872, 1992.
- [34] M. Unser, A. Aldroubi, and S. J. Schiff, "Fast implementation of the continuous wavelet transform with integer scales," *IEEE Trans. Signal Process.*, vol. 42, no. 12, pp. 3519-3523, 1994.

- [35] W. P. Kegelmeyer, J. M. Pruneda, P. D. Bourland, A. Hillis, M. V. Riggs, and M. L. Nipper, "Computer-aided mammographic screening for spiculated lesions," *Radiology*, vol. 191, no. 2, pp. 331-337, 1994.
- [36] R. C. Gonzales and R. C. Woods, *Digital Image Processing*, Addison-Wesley, Reading, MA, 1992.
- [37] J. S. Lim, *Two-Dimensional Signal and Image Processing*, Prentice Hall, Englewood Cliffs, NJ, 1990.
- [38] Y. Xing, W. Huda, A. Laine, and J. Fan, "Simulated phantom images for optimizing wavelet based image processing algorithms in mammography," in *Mathematical Methods in Medical Imaging III*, Proc. SPIE, F. L. Bookstein, J. S. Duncan, N. Lange, and D. C. Wilson, Eds., San Diego, CA, 1994, vol. 2299, pp. 207-217.
- [39] C.-M. Chang and A. Laine, "Coherence of multiscale features for enhancement of digital mammograms," *IEEE Trans. Inf. Technol. Biomed.*, vol. 3, no. 1, pp. 32-46, 1999.

List of Personnel

Iztok Koren, Ph.D., Principal Investigator